UCLouvain

École polytechnique de Louvain

Load Alleviation on a Wing Equipped with Articulated Wingtips

Author: **Florence de Schietere de Lophem**
Supervisors: **Philippe Chatelain, Matthieu Duponcheel**
Readers: **Vincent Legat, Grégoire Winckelmans**
Academic year 2021–2022
Master [120] in Mechanical Engineering

Abstract

According to recent studies, Flared Folding Wingtip devices (FFWT) can be used to increase the wingspan and efficiency of an aircraft without the need to give up the better roll rate and lesser loads of a shorter wing. First, the effect of the FWWT has been assessed. Then, the performances of a wing with FFWTs are compared with the ones of a wing with a fixed hinge, and of a baseline model from which the wingtips have been removed. The study includes the roll behaviour, a closer look at the wing root bending moment, and a simple case of turbulence. In all of these cases, the FFWT keeps its promises, reducing wing root bending moments by up to 25% and recovering most of the roll capabilities of a short wing.

Acknowledgements

I would like to express my sincere gratitude to my supervisors, Pr. Philippe Chatelain and Dr. Matthieu Duponcheel, for their guidance and assistance throughout the year.

I would like to thank Pr. Grégoire Winckelmans for his insightful comments and suggestions.

I am deeply grateful to Ignace Ransquin for his guidance at every stage of this thesis.

I want to thank them all, along with Pr. Vincent Legat, for being my readers.

Lastly, I would like to thank my family and friends for their endless support.

Nomenclature

Acronyms

AR	Aspect ratio
CAD	Computer Aided Design
FFWT	Flared Folding Wingtip
PLLT	Prandtl Lifting Line Theory
VPM	Vortex Particle-Mesh method
WRBM	Wing Root Bending Moment

Symbols

a_0	Lift slope
b	wingspan
c	Chord
C	Damping coefficient
C_{D_i}	Induced drag coefficient
C_l	Lift coefficient
C_L	Wing lift coefficient
C_m	Pitching moment
D_i	Induced drag
l	Lift per unit span
m	Mass
m_{WT}	Wingtip mass
p	Roll rate
S	Wing surface
t	Time
t^*	Dimensionless Time$\frac{U_\infty}{b}t$
T_I	Turbulence intensity
U_∞	Free stream velocity
u'	Fluctuating velocity (Reynolds decomposition)
$\overline{u}$	Mean velocity (Reynolds decomposition)
u	Total velocity (Reynolds decomposition)
w	Induced velocity

α	geometric angle of attack
α_{eff}	Effective angle of attack
α_i	Induced angle of attack
$\Gamma(y)$	Circulation
ε	Turbulent kinetic energy dissipation
θ	Fold angle
θ_C	Coast angle
Λ	Flare angle
ρ	Air density
ϕ	Roll angle

Contents

CHAPTER 1

Introduction

One of the main concerns for civil aircraft designers nowadays is to find how to increase the fuel-efficiency of their designs. A way to increase aerodynamic efficiency is to reduce aerodynamic drag. One of the main drag components, induced drag, can be reduced by increasing the aspect ratio of a wing. However, simply increasing the wingspan is not necessarily the best option, and often not conceivable for practical matters.

Indeed, airport rules, and especially the size of parking spots, put a limit on the maximal wingspan a plane can have on the ground. Moreover, increasing the span also increases the mass of the plane, for two reasons. Next to the straightforward mass increase with the increased wing size, one also has to take into account the need to increase the structural weight, to ensure enough strength to bear the additional loads, as forces acting farther away from the root result in higher bending moments. This mass increase has to be limited, as it leads to more fuel consumption. In addition, longer wings also result in less manoeuvrability, making it necessary to investigate the roll performances of a wing, as roll damping increases with increasing wingspan.

These three factors, i.e. the increase of (structural) weight, the decrease of induced drag and the effect on roll manoeuver capabilities with respect to a relatively shorter wing, can be addressed with flared folding wingtips (FFWT). These can lead to similar aerodynamic enhancements as for an increased wingspan, without impacting the structure as much.

Over the last few years, more and more research has been done around the flared folding wingtips. This thesis's goal is to create a model which will enable us to explore the possible benefits of this wingtip device by ourselves. More precisely, we will first look at the effect of the magnitude of the flare angle. This will help us to determine which angle to choose for the next steps. Then a comparison will be made between a wing with a flared hinge, the same wing with fixed hinge, and a short wing from which the folding wingtips have been removed. The goal will be to understand the impact of the configurations on the roll performances, as well as on the loads alleviation possibilities. For the latter, we will look at the wing root bending moment of the wing during straight and level cruise flight, during roll manoeuvers and during turbulence.

In the next chapter, we will explore the results of different studies that have already been performed on folding wingtips and their behaviour, in order to fully understand how they work and what they can achieve.

In Chapter 3, the focus will lie on the theory. The frame of reference will be introduced and a few concepts that are necessary for the good understanding of the rest of the thesis will be detailed. We will look at the generation of induced drag on a 3D wing, the vorticity shed into the wake and the Prandtl Lifting Line Theory.
Then follows an introduction on the roll damping, on the wing root bending moment and on the turbulence model used in this thesis.

Chapter 4 focusses on the numerics, the tools that are used and how the model evolved to its final version. We will also look at the dimensions of the model, the dimensions of the computational domain, and the ways to ensure stability of the model.

The procedures for the different analyses will be explained in Chapter 5.
In chapter 6, all the results will be analysed in more details. And finally, conclusions will be drawn in Chapter 7. The main results will be summarized, together with the questions that are still left unanswered, or that have emerged along the way.

CHAPTER 2

Related Work - State of the Art

The idea of folding wingtips is not new. Among others, it finds its application in fighter aircraft. Nowadays, in civil aircraft, the Boeing 777X is known for its folding wingtips. However, these wingtips are only meant to be actuated during ground manoeuvers. Outside of the gates, the wingtips are fully unfolded and locked until the end of the flight. This enables the aircraft to fully benefit from the reduction of induced drag by the maximized aspect ratio during flight, while respecting the size limitations set by airports on the ground.

Thus far, no civil aircraft uses freely flapping wingtips. Nonetheless, some research has been going on recently, in order to investigate the possibilities that this type of wings could offer. Most of the research has been done either numerically or experimentally in wind tunnels. Airbus changed that. With their AlbatrossONE project [1], they were the first ones to bring a reduced model of a plane with freely flapping wingtips into the air. Their inspiration was found in nature, when looking at albatrosses. These birds spend a tremendous part of their lives in the air, locking their shoulders most of the time, only unlocking them when they need better manoeuverability, or when facing instabilities in the flow.

Translated to an airplane, this behaviour is thought of to have the potential to enhance performances and efficiency. Depending on the stage of flight, the configuration of the wing could be adjusted to best meet the needs. According to recent research, in-flight use of the wingtips might help to enhance the performances on a plane, more than just by increasing the wingspan. By freeing the wingtips during gusts and turbulence, the loads on the aircraft, especially those felt at the root of the wing, can be decreased. Additionally, part of the manoeuverability lost due to the increased wingspan, especially in terms of roll, could be recovered.

The idea of the flared folding wingtip is quite straightforward. First, consider the main wing of an aircraft, on which hinges are applied to separate the base wing from the wingtips. The wingtips can fold up, with a fold angle θ. The particularity of these wings, is that the hinges are not parallel to the longitudinal axis of the plane, but are rotated by a certain angle. This is the flare angle Λ and is the key parameter for successful loads alleviation [2]. Both the flare and the fold angle are shown in Figure 2.1. It has been shown that the angle of attack of the wingtip locally decreases as the wingtip folds up [2]. For small fold angles, following equation for the change in angle of attack holds:

$$\Delta\alpha = -\arctan(\sin\Lambda\tan\theta) \tag{2.1}$$

A decrease of the angle of attack can be linked to a reduction of the loads acting on the wing, and can be achieved, as shown by Equation (2.1), by a non-zero flare angle. If the wingtip is free to rotate around its hinge, it will stabilize when an equilibrium of forces and moments is attained. The fold angle at which this is the case is defined as the coast angle θ_c.

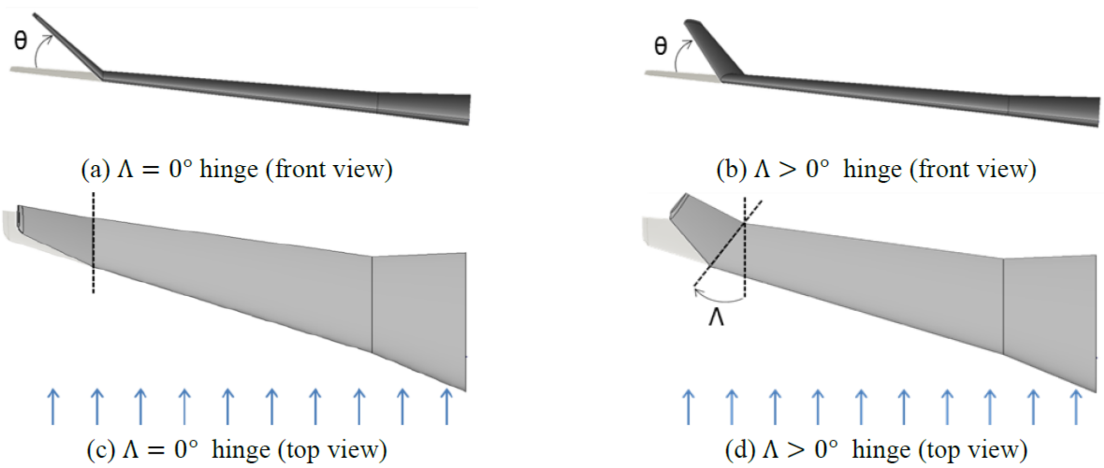

Figure 2.1: Front and top view of a wing with flared folding wingtips, showing the fold angle θ and the flare angle Λ [2].

Castrichini et al. considered different cases through numerical simulations: a wing with a fixed hinge, with a free hinge at zero and non-zero angles of attack, and the baseline model without the wingtips which acts as reference. Their goal was to find a way to increase lift (by increasing the wing surface, and especially the aspect ratio), without increasing the loads too much. The most satisfying configuration that came out of their test was a linear flared hinge, with small hinge stiffness, no hinge damping and reduced wingtip mass.

The need for the low stiffness of the hinge lay in the wingtip response to gust loads. It has been shown that the response should be quick and timed carefully in order to optimize the gust load alleviation. A quick response can be achieved through a small hinge stiffness.

A problem that arises with low hinge stiffness values is the wingtip deflection due to static trim loads, even during cruise flight, and continuous oscillations. On the one hand the stiffness should be high enough to avoid static trim deflections and continuous oscillations, but on the other hand the stiffness should be low enough to allow for efficient gust loads alleviation. Therefore, Castrichini et al. also suggested the use of non-linear hinge devices [3, 4]. A passive non-linear hinge spring is introduced, to allow wingtip deflections for larger load cases, such as gusts.

Hinge damping proved to be useful to reduce inertial loads due to the rapid movement of the wingtips. If the damping is too high, however, the load alleviation capabilities are reduced due to a too slow response. This nonlinear spring device proved to have better loads alleviation capabilities than the linear hinge, resulting even in an incremental wing root bending moment smaller than for the baseline model. Moreover, the design of their hinge made it possible for it to come back to its undeflected configuration after the gust encounter [4].

It has also been suggested that the FFWTs have the potential to improve the roll authority of the aircraft, when compared to an aircraft of same span with fixed configuration. This has been validated experimentally [5], through a wind tunnel experiment. The wingtip was unlocked during the roll manoeuver, reducing the aerodynamic roll damping and therefore enhancing the roll performance. Moreover, the peak angular acceleration of the wing was accelerated, meaning that the steady roll rate is achieved more quickly. Periodic oscillations both in fold angle and in roll rate appeared in the case of flared wings.

CHAPTER 3

Theory

The purpose of this chapter is to lay the foundations for a better understanding of what will come next.

First comes the introduction of the frame of reference that will be used throughout this work.

Then, we will take a look at the induced drag, which is the only form of drag considered in this work. The insight on induced drag does not only tell us about the fuel efficiency of an aircraft, but also gives some indication on the flow around the aircraft, with vortices shed into the wake.

This then brings us to the Prandtl Lifting Line Theory, from which we can get the circulation of distribution over the wing. From this distribution, other values and distributions can be deduced, such as the lift. This theory is what VPM, one of the numerical tools for this work, uses. More about it will come in Chapter 4.

Finally, we will also introduce the notions of aerodynamic roll damping, turbulence and wing root bending moment, all of which will be used later to assess the performances of the wing.

3.1 Reference Frame

The system of axes used throughout this paper is not the one widely used for aircraft, but the one defined in one of the computational tools, VPM, which will be introduced in Chapter 4. Here, the axes are defined as shown in Figure 3.1. The positive x-axis points vertically upwards, the z-direction follows the direction of the flow, opposite of the flight direction, and the positive y-axis points towards the left wingtip. Therefore, a positive roll angle occurs for a downward motion of the left wing, the pitch angle is negative when the nose moves up, and yaw is positive when the plane rotates to the left around the vertical x-axis. For simplification, however, the angle of attack will be considered positive when the nose of the aircraft is brought up.

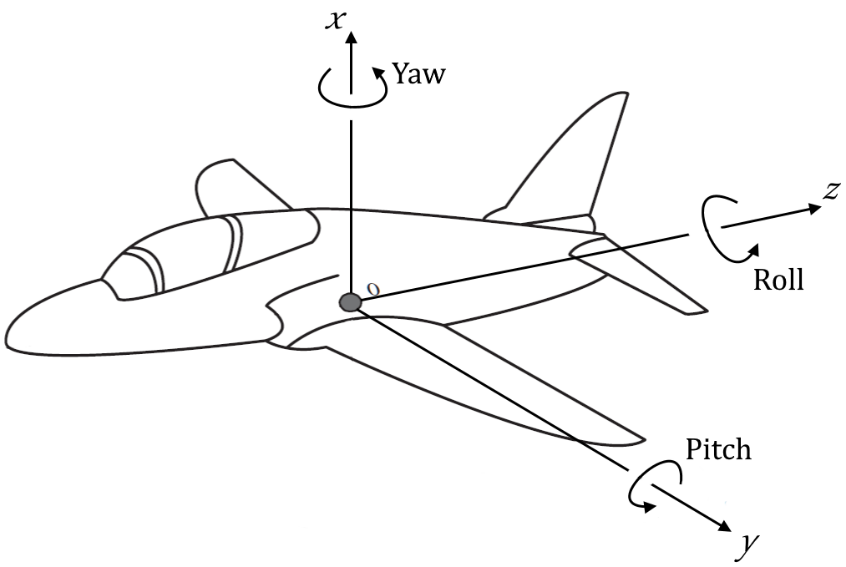

Figure 3.1: Frame of reference. Adapted from [6]

3.2 Induced Drag

Drag, the aerodynamic force working against the movement of an aircraft through the air, has several contributions, among which the so-called induced drag D_i. This form of drag appears when lift is generated on a finite object.

The flow around wings with finite span is three dimensional. Indeed, a pressure difference between top and bottom surface is needed to generate lift, resulting in a difference in the pressure field at the tips, where both surfaces meet. This pressure mismatch causes the flow to spill over from the high pressure zone on the pressure side to the low pressure zone on the suction side. This adds a spanwise velocity component to the flow, in the direction towards the root above the wing and towards the wingtip below, leading to the generation of wingtip vortices. This is shown in Figure 3.2

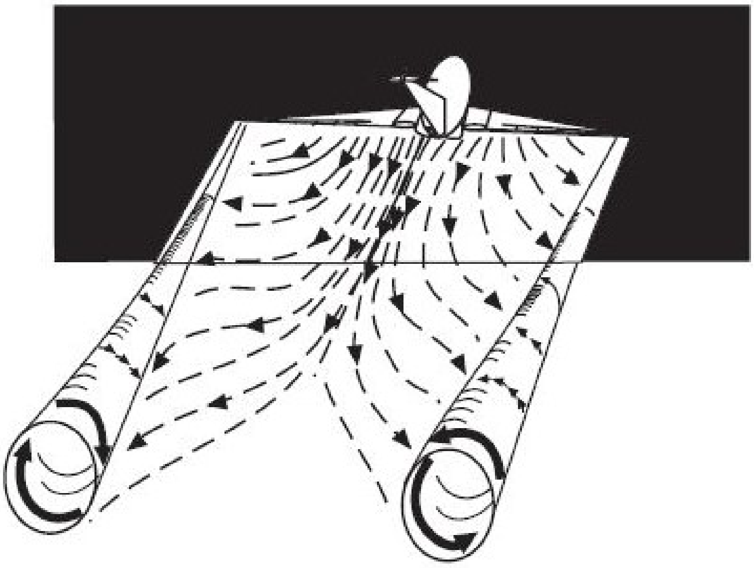

Figure 3.2: Wake vortex generation [7].

According to the Biot-Savart law, vorticity induces a flow field on its surroundings, and this velocity is inversely proportional to the distance from the vortex. The velocity induced by the wingtip vortices on the wing points vertically downwards and is therefore called the downwash velocity w. Added to the free stream velocity U_∞, the result is a total velocity vector inclined with respect to the direction of motion. This inclination is referred to as the downwash angle or the induced angle of attack α_i. As $w \ll U_\infty$, this angle is defined as follows

$$\alpha_i = \tan \frac{|w|}{U_\infty} \approx \frac{|w|}{U_\infty} \tag{3.1}$$

The effective angle of attack α_{eff} perceived by each airfoil is defined as the difference between geometric and induced angle of attack, and is therefore smaller than the geometric angle of attack of the wing.

$$\alpha_{eff} = \alpha - \alpha_i \approx \alpha - \frac{|w|}{U_\infty} \tag{3.2}$$

As can be seen in Figure 3.3, the direction of the flow perceived locally by each airfoil is tilted downwards, and by consequence the lift vector is tilted backwards. The component of the lift vector perpendicular to the flight direction is decreased, in favor of the apparition of induced drag D_i, i.e. the negative component parallel to the flight direction. Because of downwash, the lift performance of a finite wing is reduced compared to its expected value for a wing with infinite span.

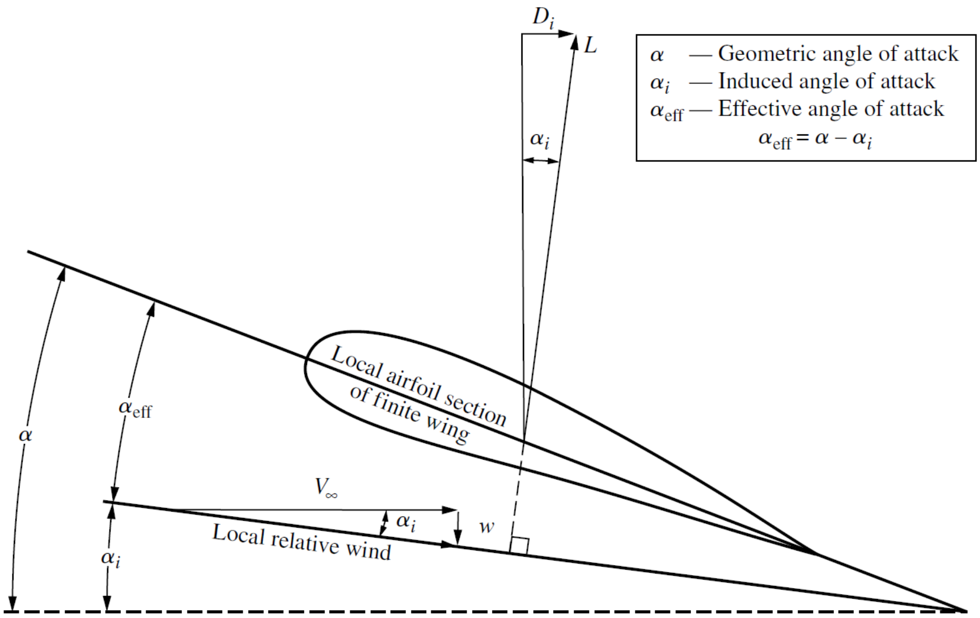

Figure 3.3: Generation of induced drag D_i [8]

From the Biot-Savart law, we know that the magnitude of the induced velocity at a given point is proportional to the inverse of the distance between the point and the core of the vortex. Therefore, the impact of the downwash becomes smaller as we move farther away from the tips, which explains why higher aspect ratio wings suffer less from induced drag.

$$C_{D_i} \propto 1/b^2 \tag{3.3}$$

3.3 Prandtl's Lifting Line Theory

For wings of finite span with high aspect ratio, Prandtl's lifting line theory can be used as a predictive model for the wing's performances. A wing, moving through a fluid and producing lift, also sheds vorticity into its wake. The wake can be thought of as a vortex sheet, rolling up on the edges, resulting in two counterrotating vortices, the wingtip vortices.

The most simple way to represent the wing and its wingtip vortices is by means of a horseshoe vortex, depicted in Figure 3.4. First, the wing is replaced by a vortex tube, a so-called bound vortex. By Helmholtz's vortex theorems, we know that a vortex tube cannot end in a fluid. It should either go on to infinity, or close back on itself creating a vortex ring. Therefore, vortex filaments are added at both edges of the bound vortex, going from these edges to infinity. As Helmholtz's vortex theorems also tell us that the circulation is constant along the vortex tube, this view implies that the circulation is constant along the wingspan, except at the wingtips where it is brought to zero, as all the vorticity is shed there. This reasoning is not realistic, as in reality the circulation varies along the span. Moreover, the velocity induced on the wing by the free trailing vortices varies in the spanwise direction, as we have learned from the Biot-Savart law. According to this law, the induced velocity would tend towards infinity at the edges.

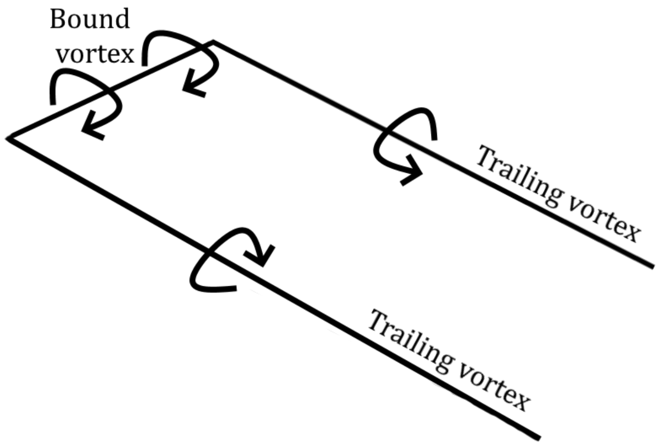

Figure 3.4: Horseshoe vortex.

To make up for this, it is possible to add up several of these horseshoe vortices, as shown in Figure 3.5. All the the bound vortices are placed on a same line, which we call the lifting line, and are centered around the center of the wing.

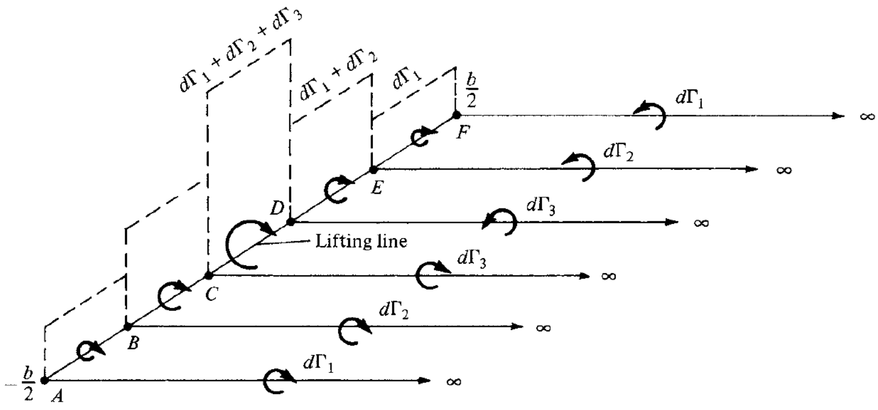

Figure 3.5: Superposition of horseshoe vortices. [8]

By superposition of an infinity of horseshoe vortices, it is possible to represent the continuous circulation distribution along the span and the whole vortex sheet that is shed into the wake, produced at the trailing edge of the wing. This is depicted in Figure 3.6. The circulation is maximal at the center of the wing and falls down progressively towards zero at the tips. The change in circulation over the span is characterised by $\frac{d\Gamma(y)}{dy}$ and is, following Helmholtz's theorems, representative of the amount of vorticity shed into the wake. The vortex sheet induces velocity on itself and tends to roll up on the edges. Further downstream, eventually only the rolled up wingtip vortices remain. They have a same vorticity magnitude, of opposite sign, and their cores are separated by a distance b_0. From the total distribution along the wingspan, it is also possible to determine the lift distribution and the total lift on the wing.

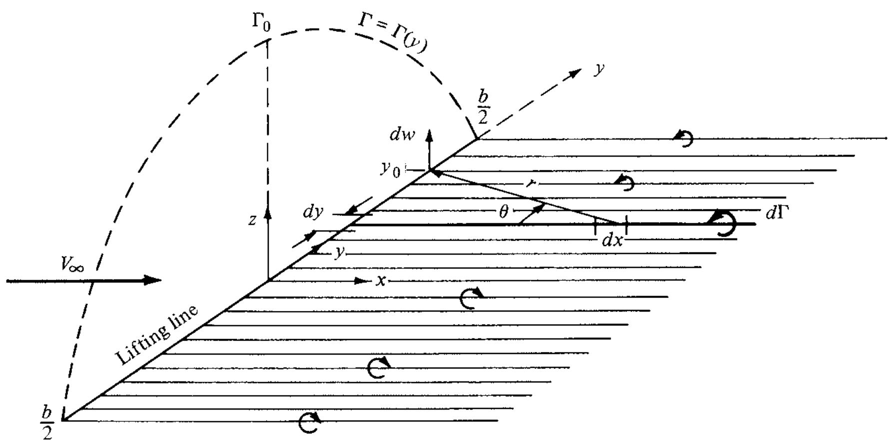

Figure 3.6: Superposition of an infinite number of horseshoe vortices along the lifting line. [8]

3.3.1 Solving for the Circulation Distribution

The lift generated on each cross-section of a wing is given by

$$l(y) = \rho U_\infty \Gamma(y) \tag{3.4}$$

while their lift coefficient C_l is

$$C_l = \frac{l(y)}{\frac{1}{2}\rho U_\infty^2 c} \tag{3.5}$$

For small angles of attack, the relation between lift coefficient and effective angle of attack can be considered to be linear. The slope, called lift slope a_0, is a constant.

$$C_l = a_0 \alpha_{eff} \tag{3.6}$$

By combining Equations (3.4), (3.5) and (3.6), following relationship can be found between the circulation and the effective angle of attack.

$$\alpha_{eff}(y) = \frac{2\Gamma(y)}{U_\infty c a_0} \tag{3.7}$$

From Equation (3.2) we have an expression for α_{eff}, depending on the induced velocity. According to the Biot-Savart law, the induced velocity, induced by the vortex sheet extending only in the downstream semi-infinite plane, is given by

$$w = -\frac{1}{4\pi}\int_{-b/2}^{b/2} \frac{1}{y-y'}\frac{d\Gamma(y')}{dy'}dy' \tag{3.8}$$

By combination of Equations (3.2), (3.7) and (3.8), Prandtl's integro-differential equation for the circulation distribution can be obtained.

$$\Gamma(y) = \frac{1}{2}U_\infty c a_0(\alpha - \frac{1}{4\pi}\int_{-b/2}^{b/2} \frac{1}{y-y'}\frac{d\Gamma(y')}{dy'}dy') \tag{3.9}$$

Through a change of variables, the circulation distribution can be expanded as a Fourier Series. The angle β is defined such that $y = \frac{b}{2}\cos\beta$. The circulation distribution can be rewritten as a sum of sines, the coefficients B_n can be defined to obtain a circulation distribution given as:

$$\Gamma(\beta) = U_\infty b \sum_{n_{odd}} B_n \sin(n\beta) \tag{3.10}$$

from which the B_n coefficients need to be computed.

Once the circulation distribution is found, the total lift on the wing can be computed as

$$L = \rho U_\infty \int_{-b/2}^{b/2} \Gamma(y)dy \tag{3.11}$$

This can be simplified as

$$L = \frac{\rho U_\infty^2}{2} b^2 \frac{\pi}{2} B_1 \tag{3.12}$$

The wing lift coefficient is defined as

$$C_L = \frac{L}{\frac{1}{2}\rho U_\infty S} \tag{3.13}$$

where S is the lifting surface of the wing.

By combining Equations (3.12) and (3.13), the corresponding lift coefficient is given by

$$C_L = \frac{\pi}{2} AR B_1 \tag{3.14}$$

with B_1 being the first coefficient of the Fourier series and AR the aspect ratio of the wing.

3.4 Aerodynamic Roll Damping

Roll motion is the rotation of the aircraft around its longitudinal axis. It can be initiated by the use of ailerons, which are control surfaces located on the main wing of an aircraft. When actuated, the effect of the ailerons is a variation of the angle of attack along the wing, resulting in a change in the lift distribution. One wing will generate less lift than the other and therefore move down while the other moves up. The wing moving down sees an upwards flow velocity component, increasing its effective angle of attack, increasing its lift. The opposite is true for the other wing.

The result is the generation of a moment countering, or damping, the controlled roll motion. The roll rate keeps accelerating, until the damping roll moment and the the controlled roll moment are at an equilibrium. Then the so called steady roll rate has been achieved.

3.5 Turbulence

Flared folding wingtips are meant to have a beneficial effect on the performances of a wing when facing flow perturbations, including turbulence. The intensity T_I of turbulence in a flow is defined as

$$T_I = \frac{\sqrt{\overline{u'u'}}}{\overline{u}} \tag{3.15}$$

Here, $\overline{u}$ and u' are defined as the mean velocity and the fluctuating velocity of the flow, by means of the Reynolds decomposition:

$$u = \overline{u} + u' \tag{3.16}$$

Turbulence can be modelled in different ways. In this thesis, the Mann Turbulence Model has been implemented, using a Mann Box. This model is characterized by three main parameters: $\alpha\varepsilon^{2/3}$, Γ and the turbulent length scale L. Γ is the degree of anisotropy of the turbulence and ranges between 0 and 1. This work will deal with an isotropic perturbation field, characterized by $\Gamma = 0$. $\alpha = 1.5$ is the von Kármán constant, and ε is the turbulent kinetic energy dissipation. Together, they characterize the intensity of the turbulence.

Values for the non dimensional turbulent kinetic energy dissipation ε^* are tabulated and known to be representative for certain turbulence intensities. Using the definition of ε^*,

$$\varepsilon^* = \frac{\varepsilon b_0}{v_0^3}, \tag{3.17}$$

it is possible to find the corresponding value for ε. The velocity v_0 is defined as

$$v_0 = \frac{\Gamma_0}{2\pi b_0} \tag{3.18}$$

with b_0 being the distance between the cores of the wingtip vortices in the far wake, and Γ_0 the maximal circulation at the center of the wing, described by

$$\Gamma_0 = \frac{mg}{\rho b_0 v_0} \tag{3.19}$$

where ρ is the density of the flow. By combining Equations (3.18) and (3.19) to get an expression for v_0, the result can be substituted into Equation (3.17) to get a value for ε.

3.6 Wing Root Bending Moment

The wing root bending moment (WRBM) of a wing is the bending moment felt at the root of the wing, the latter being the junction of the wing with the fuselage.
The moment exerted by a force on a point of reference of a structure depends on the force vector applied to the structure and the distance vector between the application point of the force and the reference point.

$$\underline{M} = \underline{x} \times \underline{F} \tag{3.20}$$

The moment at an arbitrary point on a beam embedded on one end is caused by all the forces exerted on the beam between that point and the free end of the beam. The closer we get to the root, the more of these forces need to be considered, and the longer their lever arms will be. Consequently, the moment felt at the embedded end of the beam is the highest. This can be extended to wings, where the root of the wing can be associated to the embedded end of the beam, while the wingtip corresponds to the free end.

The forces F_x applied vertically on a wing cause the wing to bend, generating a bending moment M_z around the longitudinal axis. As F_x and y are by far the biggest components of $\underline{F}$ and $\underline{x}$ respectively, it is indeed M_z that needs more of our attention to asses the enhancements a flared wing could bring in terms of structural weight. The value we are interested in is the value of the bending moment at the root, called the Wing Root Bending Moment.

$$M_{z_{root}} = WRBM = \int_{root}^{tip} y dF_x \tag{3.21}$$

When a wing grows longer, the lever arm of the distributed forces along the wing grows too, resulting in an increased bending moment. Having a higher aspect ratio wing can therefore be detrimental. The hope is for the flared wings to have a lower WRBM than the fixed wing. If so, the wings could either have a longer lifetime, or the structural weight necessary to provide enough strength could be decreased.

CHAPTER 4

Numerical Model

We will start this chapter by looking at the numerical tools, Robotran and VPM, with a brief description of how they work.
Then, we will discuss the model and all its specifications, going from a basic model to the final model.
Once the logic behind the model has been explained, the dimensions of the model can be defined, as well as some flow parameters. This is followed by a brief description of the computational domain.
To end, we will look at the stability of the airfcraft, for which we define two controllers.

4.1 Numerical Environment

For this project, the Prandtl Lifting Line Theory is used to model the wing. Instead of modeling the problem using CAD-like files and softwares, computations are performed on the basis of lifting lines, to which certain properties are attributed. A Vortex Particle-Mesh (VPM) code is linked to the multibody system integrator Robotran. Robotran takes care of the multibody dynamics of the system, linking multiple bodies through specified degrees of freedom, and integrating the forces acting on the bodies. Meanwhile, the VPM method computes the fluid dynamics part of the problem, by computing the effect of a body on the surrounding flow through Prandtl's Lifting Line Theory.

The Vortex Particle-Mesh method solves the Lagrangian formulation of the Navier-Stokes equations in terms of vorticity for incompressible flows, which is the following:

$$\begin{cases} \underline{\nabla} \cdot \underline{v} &= 0 \\ \frac{D\underline{\omega}}{Dt} &= \underline{\nabla v} \cdot \underline{\omega} + \nu \nabla^2 \underline{\omega} \end{cases}$$

The method relies on both a mesh and particles for its resolution. As the method is based on the Lifting Line theory, the idea is not to solve the flow, but to compute the effect that the wing has on the flow, as it causes circulation in the surrounding flow.

4.2 The model

The bodies in Robortan can be linked to lifting lines in the VPM code. The model defines 6 bodies in Robotran, from which one acts as the actual body (fuselage) of the aircraft, while the 5 others are linked to lifting lines to form the main wing. The center of gravity of each body has been defined at the geometrical center point of the body. The centre of gravity of the aircraft is considered to be located at the centre of the wing.

4.2.1 Lifting Lines

Usually, one lifting line is considered per lifting surface, i.e. the main wing as well as the horizontal and vertical tailplanes. For simplification, the tail is not represented in this model. However, multiple lifting lines are still considered. Figure 4.1 shows the top view of the right wing of a first model with 3 lifting lines.

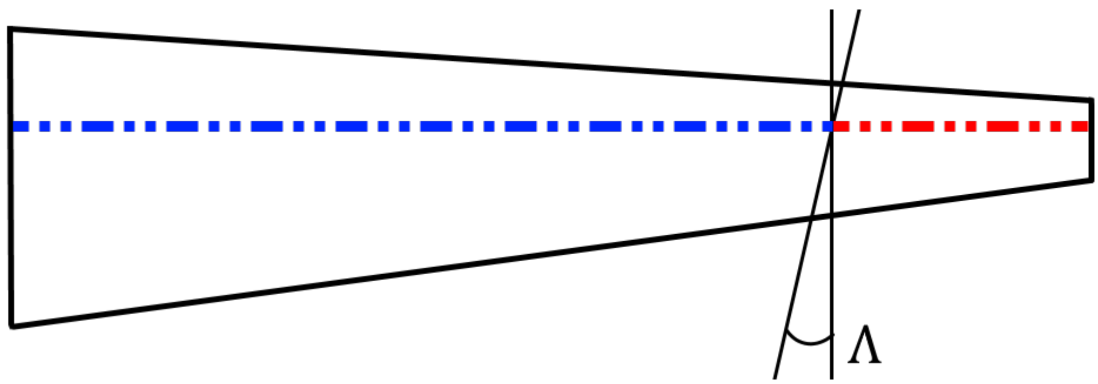

Figure 4.1: Top view of the right wing of the model with only three lifting lines.

Each wingtip (red) is modeled by its own lifting line, separated from the central part of the wing (blue) through a hinge modeled by three joints. First, a rotation around the vertical axis introduces flare into the hinge. The amplitude of this rotation is the flare angle Λ and is locked. Next comes a joint allowing the wingtip to freely fold up around the local z-axis. The wingtip never folds down lower than the horizontal plane. The rotation angle around this axis is the fold angle θ. Considering only these two rotations would result in a wingtip with sweep, even at a zero fold angle, as shown in black in Figure 4.2. To make sure that the lifting lines are correctly aligned as indicated in red, an extra rotation around the local x-axis is added. The magnitude of this third rotation is the one of the flare angle, but of opposite sign. It does not affect the fold angle directly, but affects the circulation generated by the lifting lines.

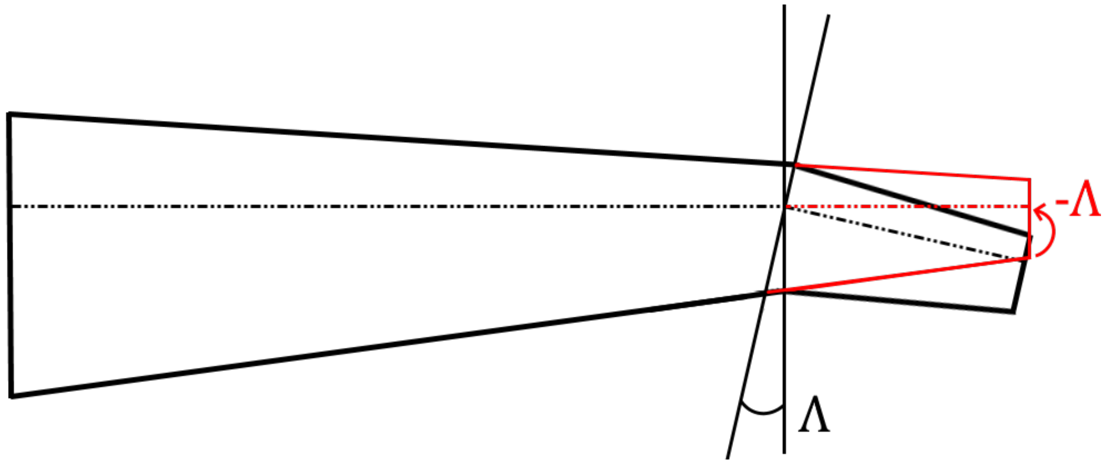

Figure 4.2: Top view at zero fold angle; (black) with wingtip sweep, (red) rectification of the wingtip sweep by adding an extra rotation around the vertical axis in the wingtip body frame.

Adding Ailerons

To be able to investigate the roll performance of the plane, multiple solutions are considered, as will be detailed in Section 6.8. One of them needs the wing to be able to take care of the roll motion by itself, without the need of an external input. To this end, two extra lifting lines are implemented, one on each side of the wing. The central lifting line is shortened, and the new lifting line is placed between the central lifting line and the hinge. This line is indicated in green in Figure 4.3. It is meant to represent the effect of ailerons on the angle of attack of the wing. In practice, roll motion is achieved by a deflection of the ailerons. The result of this deflection, usually positive on one wing and negative on the other, is a change in local angle of attack. This change results in a change of lift. An imbalance of lift distribution is created, resulting in a motion of roll. Here, instead of the aileron deflection, it is the resulting change in angle of attack that is used as a parameter for the model. This brings the total number of lifting lines up to 5.

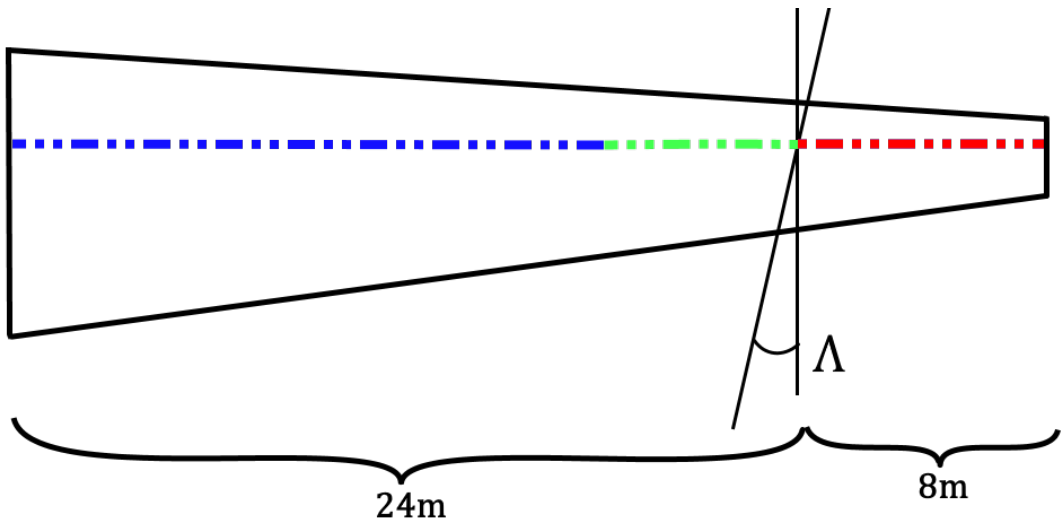

Figure 4.3: Top view of the semi-span. Dotted lines represent the lifting lines of (blue) the central part of the wing, (green) the ailerons, (red) the wingtips.

4.2.2 Planform

Over the whole duration of this work, three main configurations will be considered and compared. We will call them the fixed wing, the flared wing and the short wing. The whole model with the 5 lifting lines and fixed hinge represents the fixed wing. When the wingtips are free to fold around the hinge, we are looking at the flared wing. The short wing is equivalent to the fixed wing from which the wingtips are removed. Only the 3 central lifting lines are used in the model of this last configuration, and this will also be referred to as the base wing.

As the wing planform for both the fixed wing and the short wing have to be realistic, the elliptical wing was left out of the equation. The tapered/trapezoidal wing was chosen above the rectangular wing in order to limit the magnitude of the discontinuity at the wingtips, and over a triangular wing in order to provide a better overall circulation distribution. One needs to keep in mind that this leads to a mismatch in taper ratio between fixed wing (0.2) and short wing (0.4).

4.2.3 Dimensions

The model is roughly based on the dimensions of an Airbus A350. The wing has a trapezoidal shape and a taper ratio of 0.2. The shape of the wing, taking the quarter-chord location of the lifting lines into account, has already been shown in Figure 4.3. The base wing has a span of 48m, and each wingtip has a length of 8m, bringing the total span up to $b =$ 64m. The total surface is $S = 442m^2$. A total mass of 275 tonnes is given to the plane, from which 15% is attributed to the wing. In the standard configuration, both wingtips have a mass of 1238kg. The flow has a free stream velocity of $U_\infty = 250m/s$

4.2.4 Computational domain

The computational domain has a size of $b \times 2b \times 8b$, where b is the total wingspan. The location of the wing in the domain is fixed in order to have half a wingspan between the wing and the boundaries in both spanwise and both vertical directions, as well as one full wingspan in front of the wing and 7 spans in the wake. The mesh contains 64 nodes per span.

4.2.5 Control

Among the parameters to specify in the VPM model, the lift slope $\frac{dC_l}{d\alpha}$ for the profiles of the wing is set to be equal to 2π. The model considers no pitching moment coefficient C_m and no other drag components than the induced drag. When C_m is different from zero, it can play a role in the stability of an aircraft. In addition, the model considers only the main wing, not the tail.

In practice, the stability of an aircraft is ensured through its control surfaces, from which some are located on the tail. It is therefore necessary to come up with other ways to provide stability to the aircraft. Only pitch and roll are considered for that matter, as the yaw degree of freedom is never let free in this study.

As there is no dihedral, the roll stability is ensured through a controller, calling upon the ailerons to deflect in order to bring the roll angle ϕ back to zero after executing a roll manoeuver. A second controller is implemented for the pitch. The pitch angle is adjusted in order to keep the vertical acceleration at equilibrium around zero. Hereby, the goal is to achieve a constant lift, equal to the weight of the aircraft throughout the flight, in order to obtain level flight. By defining θ_p as the pitch angle, with superscript n indicating the current time step and $n+1$ the next time step, the pitch controller is defined as:

$$\theta_p^{n+1} = \theta_p^n + K_p(\ddot{x}_{ref} - \ddot{x}^n) \tag{4.1}$$

K_p is the gain factor associated to the pitch controller. Here, the reference vertical acceleration is $\ddot{x}_{ref} = 0$.

If δ is the deflection angle of the ailerons, then the roll controller is defined as

$$\delta^{n+1} = \delta^n + \frac{\Delta t}{\tau}(K_r(\phi_{ref} - \phi^n) - \delta^n) \tag{4.2}$$

K_r is the gain factor associated to the roll controller, τ is a time constant and $\phi_{ref} = 0°$ is the reference roll angle, which the controller tries to achieve.

CHAPTER 5

Procedure

In this chapter, the methods used to compare the different wing configurations will be detailed. Two types of simulations can be considered. On the one hand, the behaviour and performances of the flared wing need to be compared to the ones of the fixed and short wings. To this end, a flare angle of 20° will be considered, as will be justified in Chapter 6. On the other hand, the impact of the magnitude of the flare angle will be investigated.

A first batch of simulations is run in order to obtain the angle of attack necessary for each configuration to achieve level flight. Once these angles of attack are retrieved, all other simulations are run using them as input. Except for the simulations with roll, the pitch controller is activated in order to stay at level flight during the whole simulation.

In order to verify the reliability of the model, the circulation distribution and wing lift coefficient of the fixed wing are compared with the theory. The theoretical values can be obtained as described in Section 3.3.1, when introducing the Prandtl lifting line theory. The quality of the results obtained for the simulations at 64 nodes per wingspan will be evaluated for the flared wing by a comparison with a more refined mesh with 128 nodes per wingspan.

Next, the behaviours and performances of the different configurations will be assessed for a uniform inflow with free stream velocity $U_\infty = 250 m/s$. A first comparison will be made between the flared, fixed and short wings on the basis of the impact of the configuration on the distribution of circulation, the wake, the induced velocity, the effective and geometric angles of attack and the loads.

A look at the lift distributions for the different configurations can tell more about the loads to be expected at the root of the wing. By taking into account both the vertical aerodynamic force and the vertical gravity force, the bending moment distribution and the wing root bending moment can be assessed, as described in Section 3.6.

Different cases of given flow velocity, angle of attack and wingtip mass will be considered for the flared wing, as well as the effect of the amplitude of the flare angle on the behaviour of the wing. The results to be compared are the evolution of the fold angle and its corresponding coast angle, the amplitude of the wing root bending moment, and the variation of both effective and geometric angle of attack.

The roll behaviour of the different wing configurations also needs to be considered. When imposing a given roll rate on the wings, the bending moment at the root can be assessed and compared. The effect of roll damping can be observed and compared from one wing configuration to another when a torque is applied, either through an external application, or through a deflection of the ailerons.

Another situation for which it is crucial to determine and compare the wing root bending moment values, is during turbulence. As explained in Section 3.5, the turbulence is modelled using Mann Boxes. Two non-zero turbulence intensities are considered and compared with the zero turbulence case. For these simulations, both controllers are activated, and all degrees of freedom of the aircraft are set to zero, except for the pitch and roll angle.

CHAPTER 6

Results and Analysis

The results of the numerical simulations are presented and discussed in this chapter. The main goal is to understand what the effect is of a flared hinge and of the magnitude of its flare angle on the behaviour of the wing. A first part of the understanding is achieved by a parametrical study. Later, more specific cases of roll and turbulence are considered to assess the performances in manoeuvrability and load alleviation capability.

6.1 Comparison with the Theory

6.1.1 Circulation Distribution over the Fixed Wing

Figure 6.1 shows the circulation distribution over the fixed wing, comparing the result according to the Prandtl lifting line theory to the result obtained through simulation. The theoretical distribution is computed as described in Section 3.3.1, through a sum of contributions described by the Fourier Series, on the basis of properties such as the taper ratio, the span and the aspect ratio of the wing. Both distributions do not coincide exactly. The main difference can be seen close to the wingtips, where the circulation decreases more gradually in the theoretical case. In addition, numerical noise can be noticed close to the edges of the wing, due to the steep gradient of circulation distribution occurring at the edges. This might be linked to the values of circulation distribution that do not decrease fast enough at the tips, combined with the numerical noise around the edges.

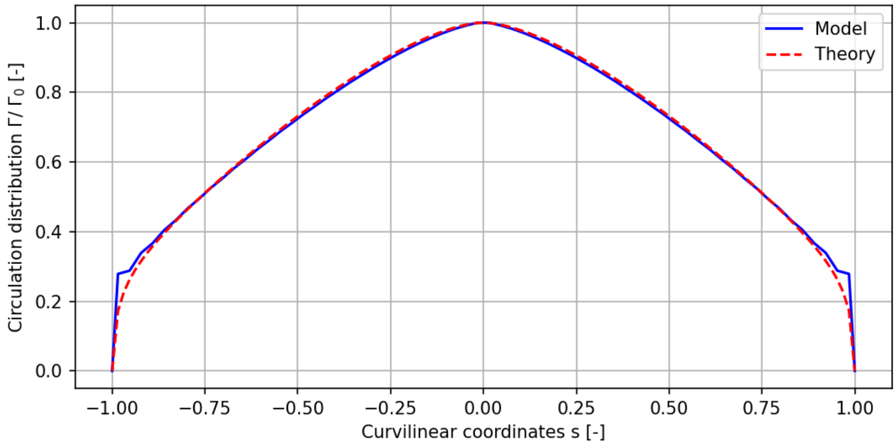

Figure 6.1: Circulation distribution of the fixed wing. Comparing the theoretical distribution with the numerical distribution.

6.1.2 Lift Coefficient

The theoretical value of the wing lift coefficient C_L can be computed from the B_1 factor of the Prandtl lifting line theory, as described by Equation (3.14). The dependency of the lift coefficient on the angle of attack is depicted in Figure 6.2.
The theoretical value is compared to the value obtained numerically. The blue dot represents the C_L at the angle of attack at which lift and weight balance each other out. The lift coefficient of the model is found to be higher than predicted by the theory.

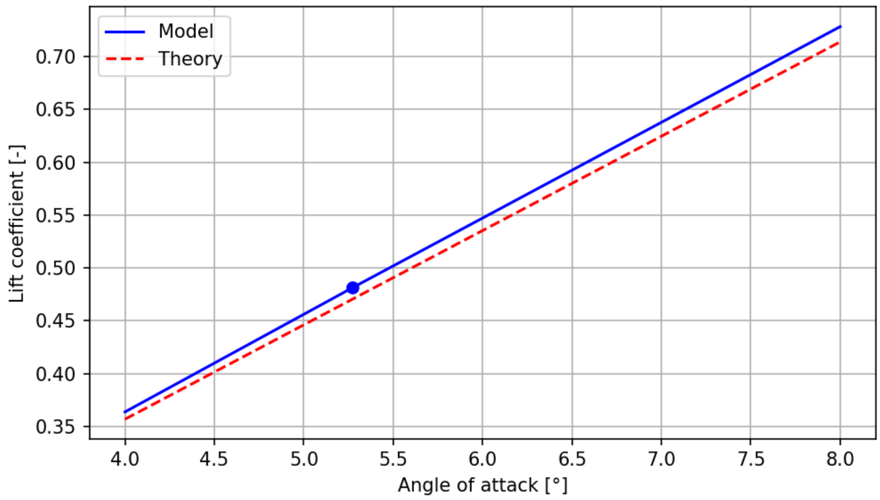

Figure 6.2: Wing lift coefficient of the fixed wing as a function of the angle of attack. Comparing the theoretical with the numerical lift coefficient.

6.2 Comparison of the Three Configurations

6.2.1 Circulation

Figure 6.3 shows the circulation distributions for flared, fixed and short wings. For the fixed and short wings, the circulation is distributed quite evenly over their whole respective spans, while a great drop of circulation occurs around the hinges of the flared wing.

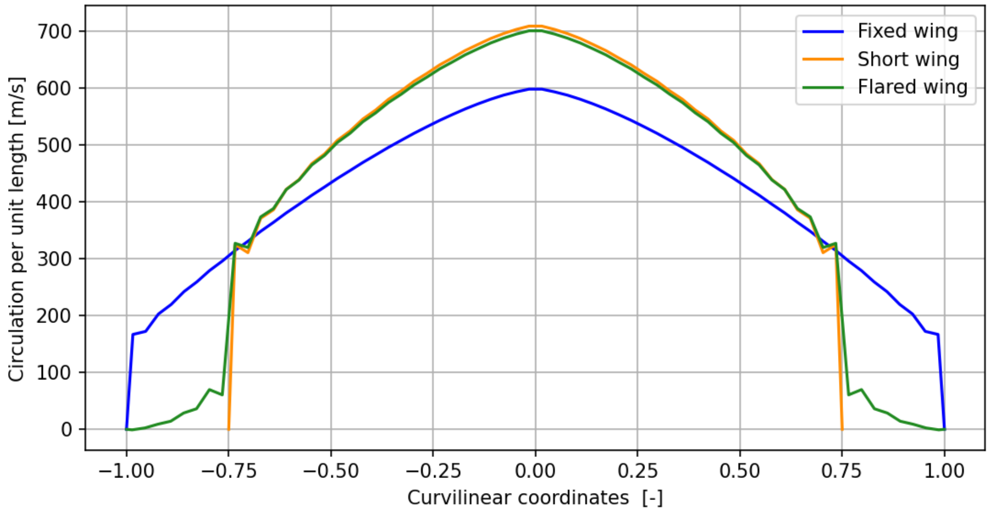

Figure 6.3: Circulation distribution along the wing for the three base configurations.

The slope of the circulation distribution is an image of the vorticity shed into the wake. The location where the roll up of the vortex sheet happens coincides with the place where the biggest drop in the circulation distribution occurs. This is confirmed by Figure 6.4, showing the wake of the three main configurations. For the fixed and short wings, the vortex sheet rolls up around the wingtips. In the case of the flared wing however, the main roll up happens close to the hinge. This means that the induced velocity on the flared folding wingtips points vertically upwards. We will call this upwash, in contrast to the downwash defined in Section 3.2. This effect is shown in Figure 6.5.

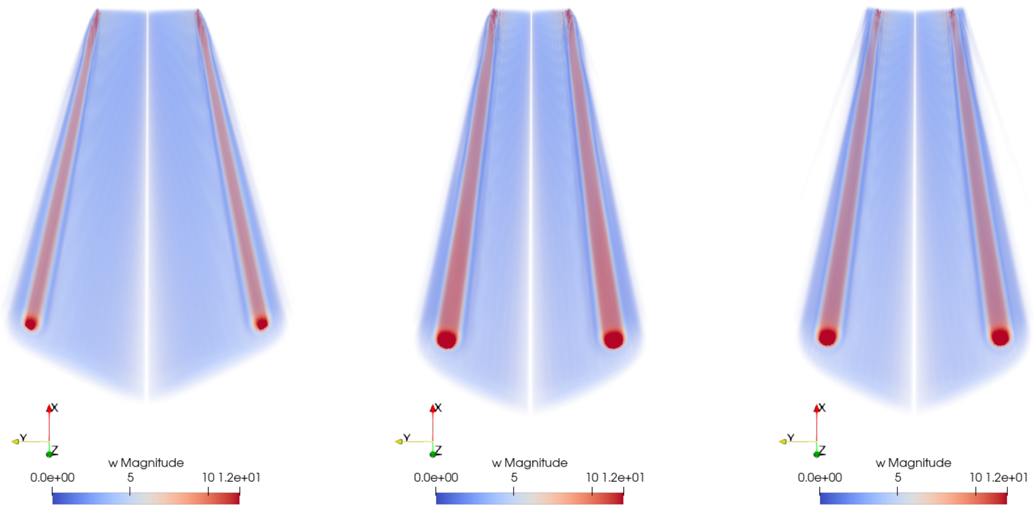

(a) Fixed wing. (b) Short wing. (c) Flared wing.

Figure 6.4: Wakes of the three base configurations during level flight.

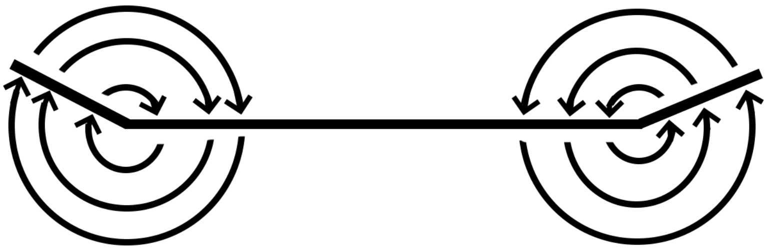

Figure 6.5: Main roll-up vortices in the wake are shifted towards the hinges, resulting in downwash on the base wing but upwash on the wingtips.

It is also possible to see the increase in magnitude and decrease in distance between the vortex roll ups of the flared and short wings compared to the fixed wing. This is emphasized in Figure 6.6a, showing the superposition of the wakes of the flared and of the fixed wing. Figure 6.6b shows that there is a slight shift between the wakes of the short wing and of the flared wing. The cores of the vortices are located a little higher and farther away from each other in the case of the flared wing.

Figure 6.3 also shows that the numerical noise that could already be observed on the edges of the fixed wing in Figure 6.1, can also be found on the edges of the short wing. For the flared wing, this noise is present close to the hinge on the base wing, as well as all over the wingtip.

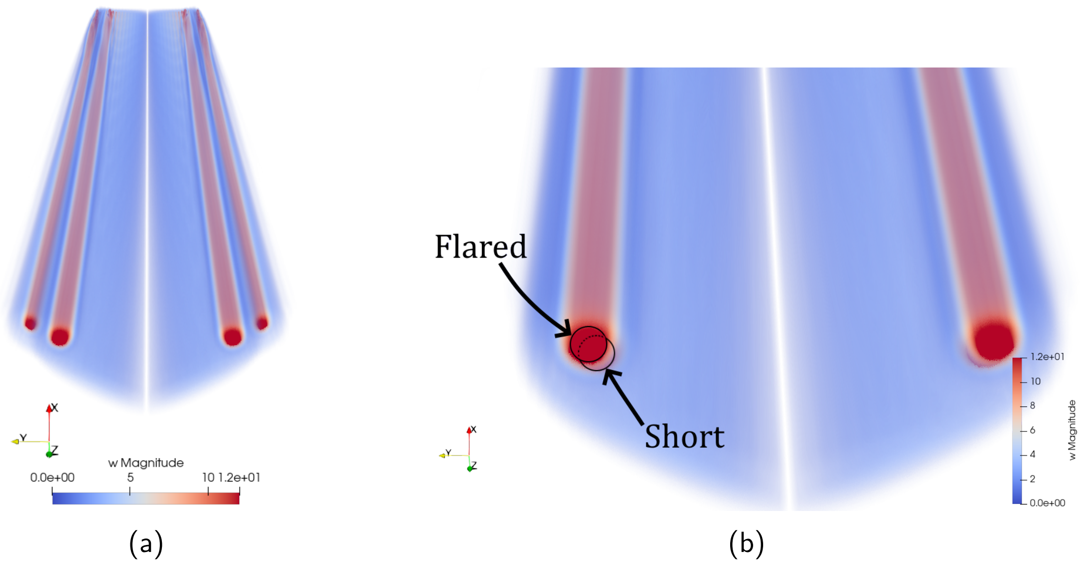

Figure 6.6: Superposition of wakes of (a) fixed and flared wing, (b) short and flared wing.

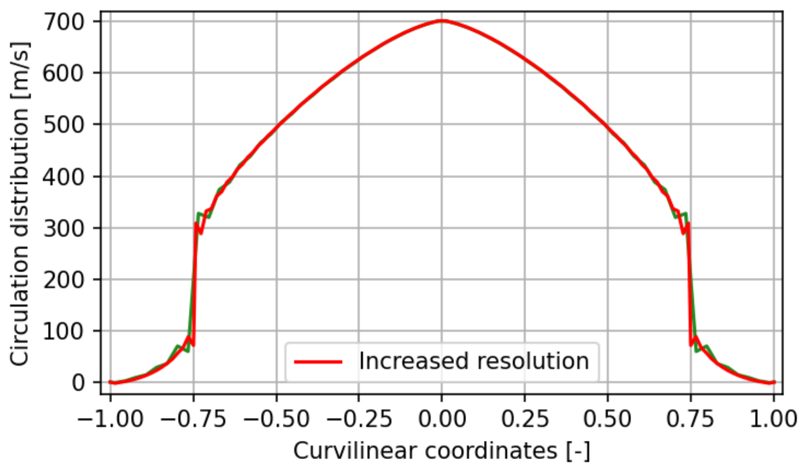

Figure 6.7: Circulation distribution obtained with a finer mesh, with twice as many points in every direction, compared to the result obtained with the regular mesh.

The red curve in Figure 6.7 is obtained by doubling the amount of mesh grid points in every direction. This brings the number of points from 64 up to 128 per wingspan. The result does give a smoother distribution around the hinge and especially on the wingtips. However, the additional computational cost required is considerable for a small gain and is not deepened in this thesis.

6.2.2 Angle of Attack and Induced Velocity

To get to a same level of lift, the three configurations need to fly at different angles of attack, as shown in Table 6.1. The values for the short and the flared wing are quite similar, and significantly larger than for the fixed wing.

Fixed	5.27°
Short	6.39°
Flared	6.32°

Table 6.1: Geometric angle of attack to achieve an equilibrium between lift and weight.

It is important to emphasize that the geometric angle of attack of a flared wing is not constant over the whole wingspan. Table 6.1 shows the angle of attack of the base wing, but as indicated in Section 2, the geometric angle of attack of the wingtip is reduced locally when the wingtip folds up. The difference depends on both the flare and the fold angle.

The effective angle of attack and effective velocity perceived by the wing are obtained as a result of the simulation. The longitudinal and vertical components of the effective velocity vector are shown for the flared wing in Figure 6.8. Equation (3.1) tells us that it is possible to compute the induced angle of attack from these two components. By substituting the effective and the induced angle of attack into Equation (3.2), we can find the geometric angle of attack.

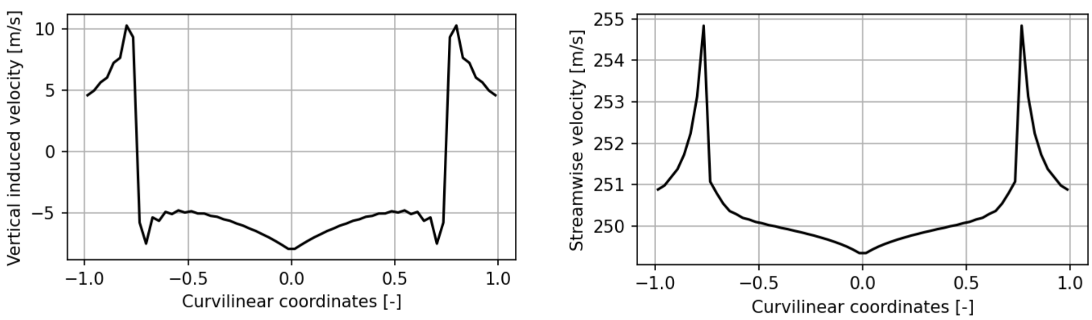

Figure 6.8: Distribution of (left) vertical and (right) streamwise velocity as seen by the wing

In the case of a flared wing, the vortex roll-up in the wake is located closer to the hinge than to the wingtip. The vertical induced velocity on the base wing is still pointing downwards. On the wingtips, however, this induced velocity points upwards.

This is what we showed in Figure 6.5. It is confirmed by Figure 6.8, from which we can see that the magnitude of the vertical component of this induced velocity is quite significant.

By adding up the induced and the effective angle of attack, the geometric angle of attack can be retrieved. The distribution found this way almost coincides with the value found theoretically through Equation (2.1), which was valid for small fold angles. Looking in more detail at these angles of attack for the flared wing in Figure 6.9, we see that the geometric angle of attack is negative on the wingtips. Nevertheless, the induced velocity is such that even on the wingtips the effective angle of attack is positive and a positive lift force can be generated.

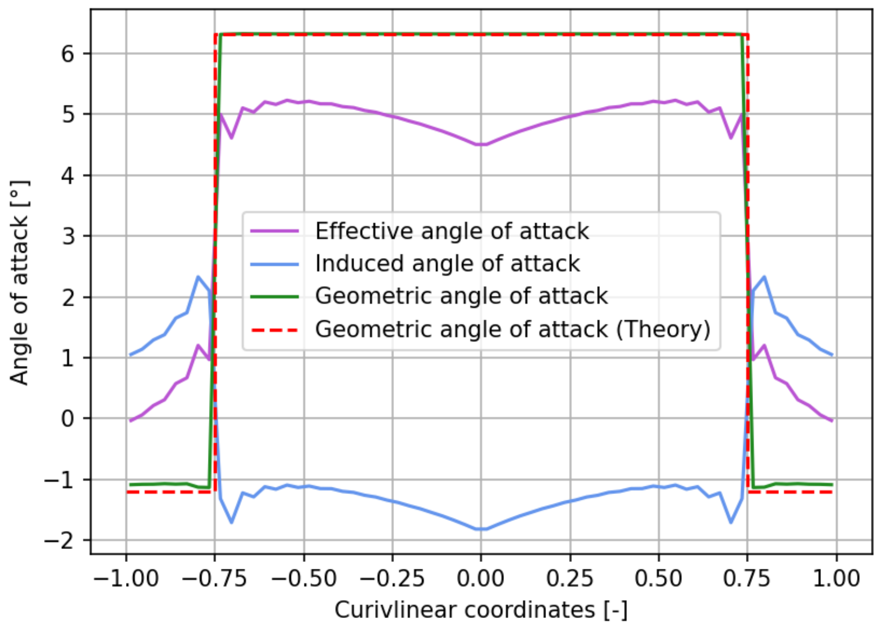

Figure 6.9: Summary of the different angles of attacks and the relations between them.

6.2.3 Loads

Lift and Bending Moment

The distribution of vertical aerodynamic force acting on the wing is shown in Figure 6.10a.

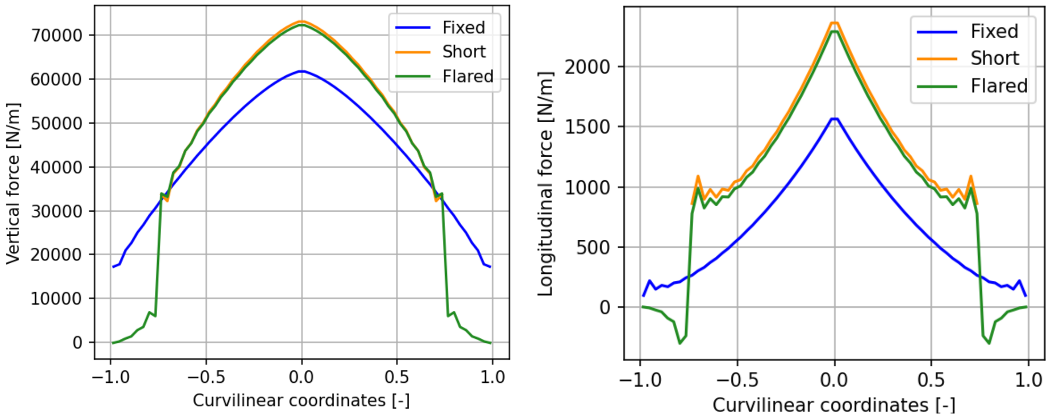

(a) Vertical lift distribution.

(b) Horizontal drag distribution.

Figure 6.10

The lift distribution over the central part of the flared wing is slightly lower than for the short wing, as the wingtips can carry part of the load. But the lift generated by the wingtips also needs to cover the extra mass of the wingtips. Due to the free hinge, however, the wingtips of the flared wing cannot carry as much load as those of the fixed wing. Compared to the two other configurations, the result for the fixed wing has a significantly smaller value per unit span, even along the base wing, Consequently, the majority of the loads on the flared wing are located closer to the wing root than for the fixed wing, resulting in a relatively lower bending moment at the root. This is beneficial in terms of structural strength demanded at the root.

Although the contribution of the gravitational force is much lower than the contribution of the aerodynamic force, both need to be considered to compute the bending moment on the wing. For each part of the wing, the gravitational force distribution is approximated by a linear distribution of the weight of the body over the length of the body. The distribution of aerodynamic force results from the simulations and is shown in Figure 6.10a. Adding up both contributions gives the net vertical force acting on the wing, which is used to compute the bending moment on the wing as described in Section 3.6.

The bending moment distribution along the wings can be seen in Figure 6.11. The hinge is located at three quarter of the semi-span, where the loads on the short wing end. The contribution to the wing root bending moment from the loads carried by the wingtip is almost negligible for the flared wing, not for the fixed wing.

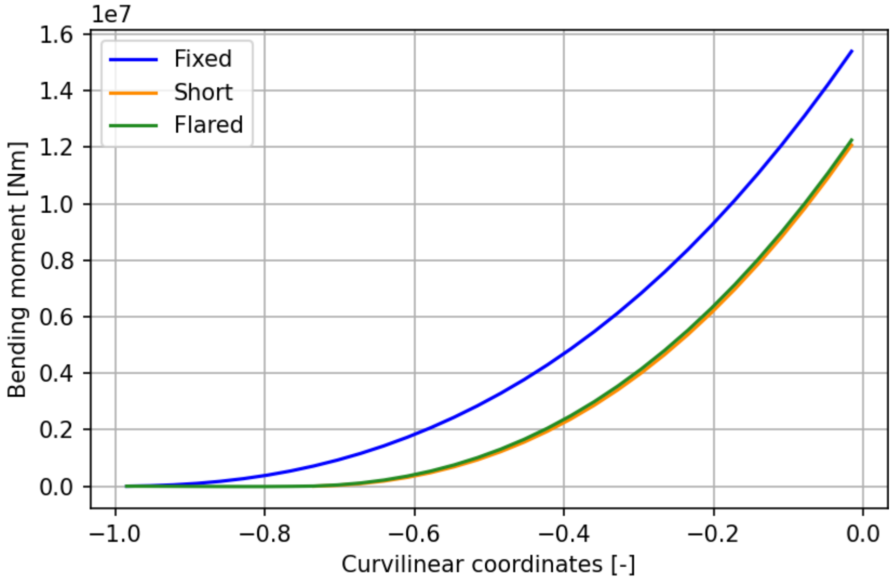

Figure 6.11: Distribution of bending moment along the wing.

The wing root bending moment of the flared wing is only slightly higher than the one of the short wing (101.4%), but considerably smaller than in the fixed case (80.4%).

Drag

The induced drag over a wing decreases with the increase of aspect ratio, which explains the clear difference in values between short and fixed wings. Figure 6.10b shows that the induced drag distribution along the base wing of the flared wing is similar to the one of the short wing, even though slightly lower. At the wingtips, the drag drops to a mainly negative value, indicating a force actually pushing the aircraft forward instead of pulling it back. This can be explained by looking at the angle of attack, the induced velocity (downwash on base wing, upwash on wingtips) and the theory of induced drag as explained in Section 3.2. As we have seen in Section 6.2.2, the geometric angle of attack on the wingtips is negative. Due to the position of the roll up of the vortex sheet, around the hinges, the wingtips are affected by an upwash, instead of downwash. This upwash increases the value of the effective angle of attack. Consequently, instead of tilting the force arrow backwards as is the case for downwash, it now tilts it forward, making the induced drag component pointing in the direction of flight of the aircraft. This relation is shown on Figure 6.12.

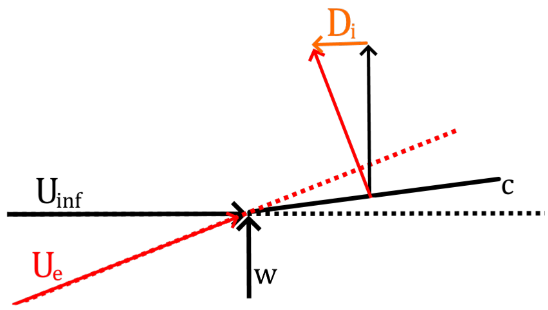

Figure 6.12: Generation of negative induced drag on the wingtips.

As a result, unlike the base wing, the wingtips have a lift vector tilted forwards Therefore, the induced drag present on the wingtips is negative, and actually pushes the plane in the direction of motion.

6.3 Effect of the Flare Angle

Investigating the flare angle Λ is a crucial step of this work, as the results will show which flare angle one might want to use for further investigation, in order to achieve the best possible results. The goal is of course to try to find the configuration leading to the best aerodynamic and structural performances.

6.3.1 Effect on the Fold Angle

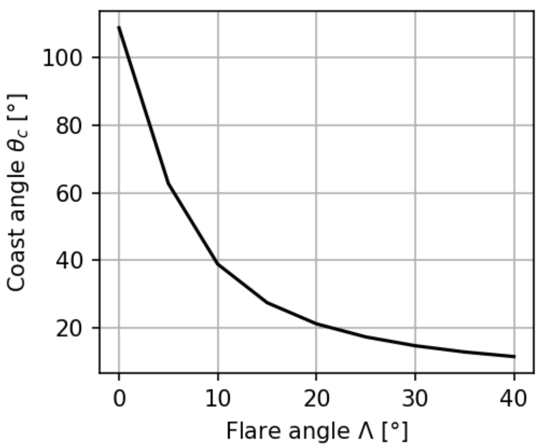

Figure 6.13: Coast angle as a function of the flared angle.

As shown in Figure 6.13, a wingtip with a smaller flare angle folds up to a higher stabilized fold angle θ_C.

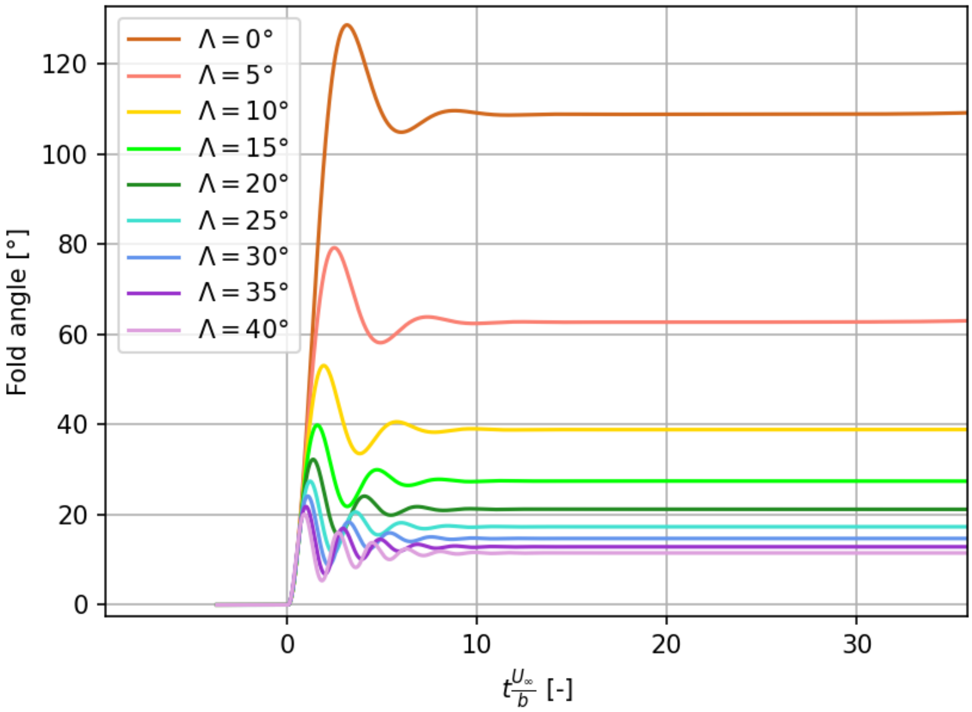

Figure 6.14: Evolution over time of the fold angle as a function of the flared angle. The time is made non-dimensional, expressed as the amount of wingspan the wing has travelled.

Figure 6.14 shows the evolution in time of the wingtip fold angle, as it tries to stabilize from a zero fold angle up to the coast angle, depending on its flare angle. Both wingtips fold up in a perfectly symmetric way. The higher the flare angle, the lower the fold angle, but the more the wingtips oscillate before reaching equilibrium. These oscillations should be limited, as they enhance fatigue of the structure.

6.3.2 Effect on the Loads

The distribution of vertical force on the flared wing is shown in Figure 6.15a. It can be seen that the distribution varies somewhat with the flare angle, but only to a certain extend. This is confirmed by the evolution of the wing root bending moment as a function of the flare angle, depicted on Figure 6.15b.

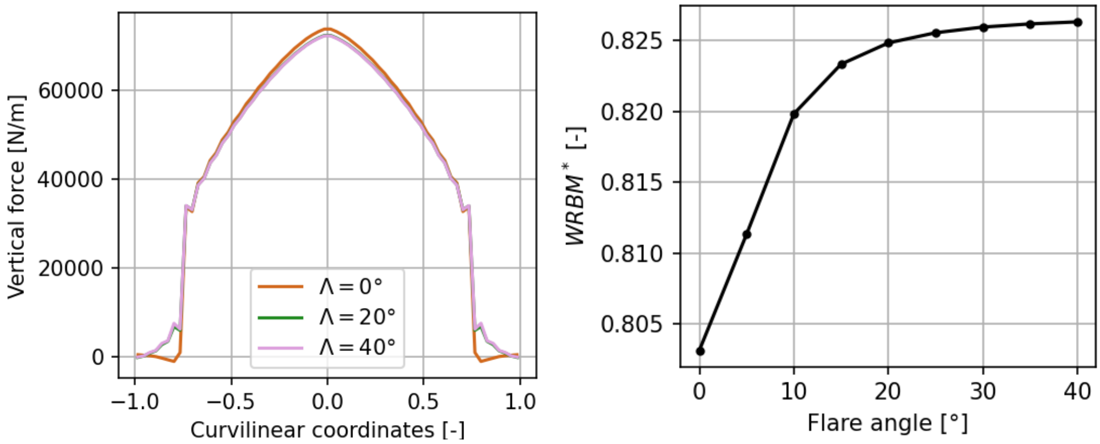

(a) (b)

Figure 6.15: As a function of the flare angle (a) the lift distribution over the wing; (b) the wing root bending moment of the flared wing normalized by the wing root bending moment of the fixed wing.

At a higher flare angle, the wingtip can carry relatively more of the vertical load, meaning that the force acting on the wing is more spread out. Consequently, the wing root bending moment increases with the flare angle, thereby slightly decreasing the load alleviation. However, the values for the WRBM are still way below the values obtained for the fixed wing.

Lift to drag ratio

Considering the different scenarios at a same level of lift, the lift to drag ratio is dictated by the induced drag generated for each case. As we have seen, the induced drag decreases with increasing flare angle. Therefore, a higher flare angle will result in a higher lift to drag ratio, up to some extend, as shown in Figure 6.16b.

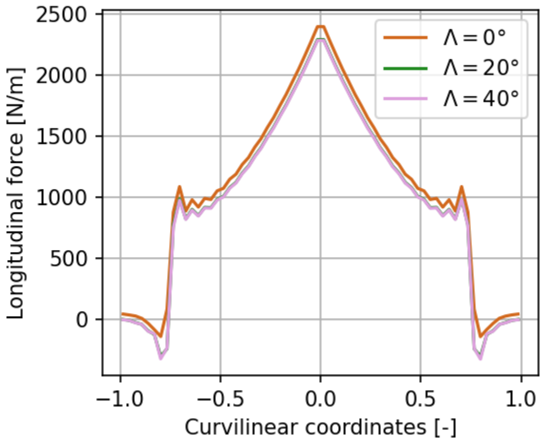

(a)

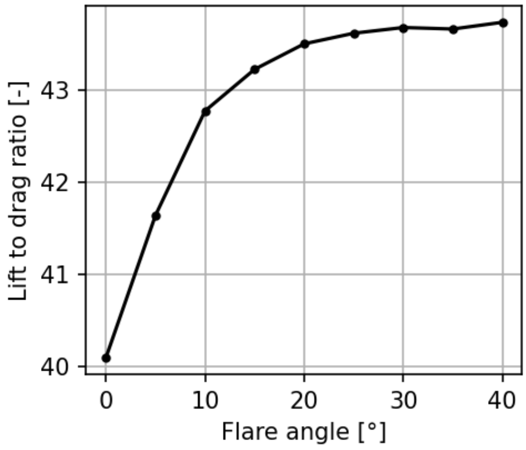

(b)

Figure 6.16: As a function of the flare angle (a) the drag distribution over the wing; (b) the lift to drag ratio.

6.3.3 Effect on the Angle of Attack

Geometric Angle of Attack

As the flare angle increases, we have seen in Section 6.3.2 that the lift generation is spread out more over the whole span of the wing. This means that the part of lift that needs to be generated by the base wing is reduced, and therefore that the angle of attack is relatively lower. This tendency is described by Figure 6.17.

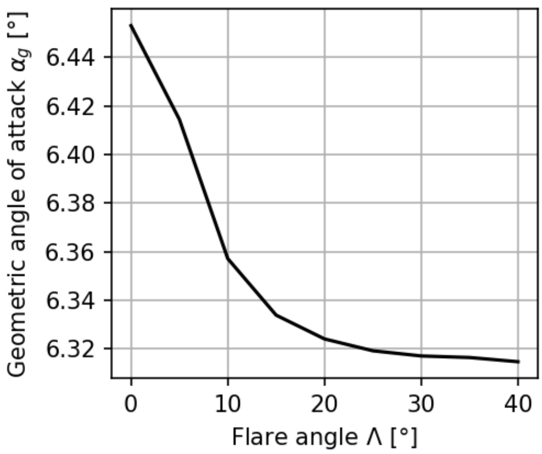

Figure 6.17: Geometric angle of attack of the base wing of the flared wing necessary to achieve level flight.

Effective angle of attack

On the wingtips, the effective angle of attack is relatively higher for higher flare angles. This is in accordance with the observation that the wingtips produce relatively more lift for higher flare angles.

6.3.4 Choosing a Good Flare Angle

Now that we have seen the different effects of the amplitude of the flare angle, it is time to evaluate which values of Λ or better than other. We have seen that an increase on flare angle results in a decrease of fold angle, leading to a longer aspect ratio, coupled to a higher lift to drag ratio. However, these value tend towards a plateau, which means that for values of 20° and more, the benefit does not very much. Beside the positive aspects of increasing the fold angle, we should else consider the increase of wing root bending moment due to the fact that the loads are more spread out. In addition, we have seen that the fold angles need more time and more oscillations before reaching their stabilized values. A good compromise can be found for agles around 20-25°. Therefore, when comparing one single flared wing with the short and fixed wings, we will consider a flared hinge with flare angle $\Lambda = 20°$.

6.4 Effect of the Angle of Attack

The effect of the angle of attack α on the flared wing is assessed by imposing different geometric angles of attack to a wing with a flare angle $\Lambda = 20°$.

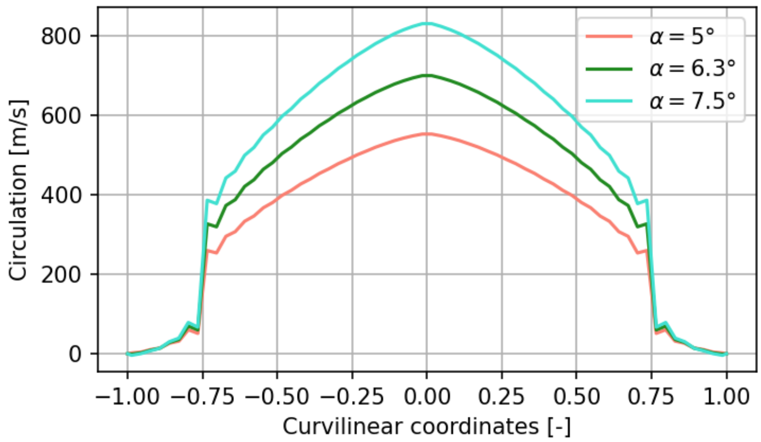

Figure 6.18: Circulation distribution along the wingspan for varying angles of attack.

As would be the case for any wing, the circulation distribution increases together with the angle of attack. This is shown in Figure 6.18. Moreover, Figure 6.19 shows that the wingtips stabilize at a higher fold angle.

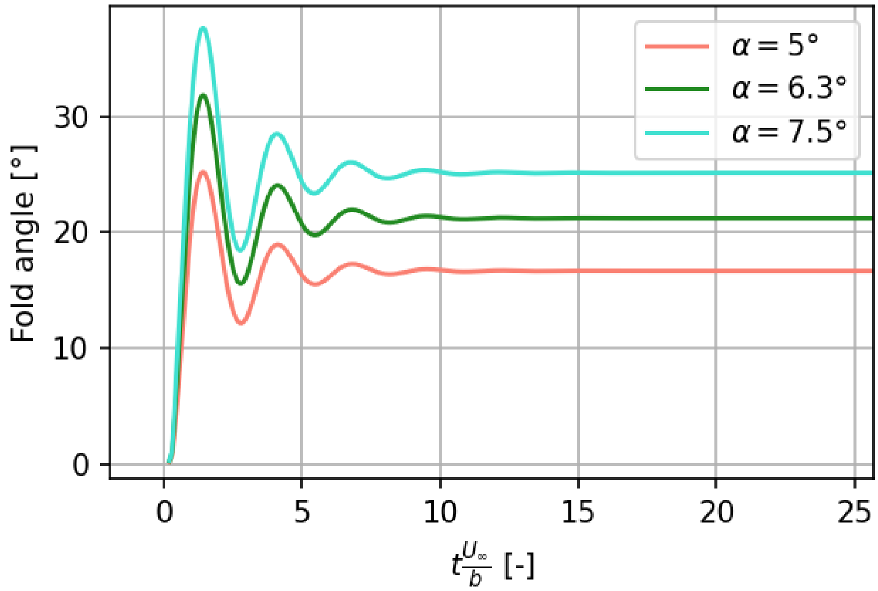

Figure 6.19: Evolution of the fold angle for different geometric angles of attack.

6.5 Effect of the Flow Speed

6.5.1 At a Same Angle of Attack

When comparing the results for free stream velocities $U_\infty = 200$, 250 and 300 $\frac{m}{s}$ at an angle of attack of 6.32° in Figure 6.20, the wingtip folds up to a higher folding angle with higher free stream velocity. The dynamics in time, expressed as the amount of spans travelled by the aircraft $t^* = t\frac{U_\infty}{b}$, do not change from one flow velocity to another.

Figure 6.21 shows that the effective angle of attack on the base wing does not change with the flow speed. As the geometric angle of attack of that part of the wing is fixed from one case to another, this means that the induced angle of attack does not change either. The induced downwash velocity is linearly proportional to the flow stream velocity. On the wingtips, however, the angle of attack changes. The proportionality between induced and free stream velocity does not change here either, but the geometric angle of attack of the wingtip is decreased as it folds up.

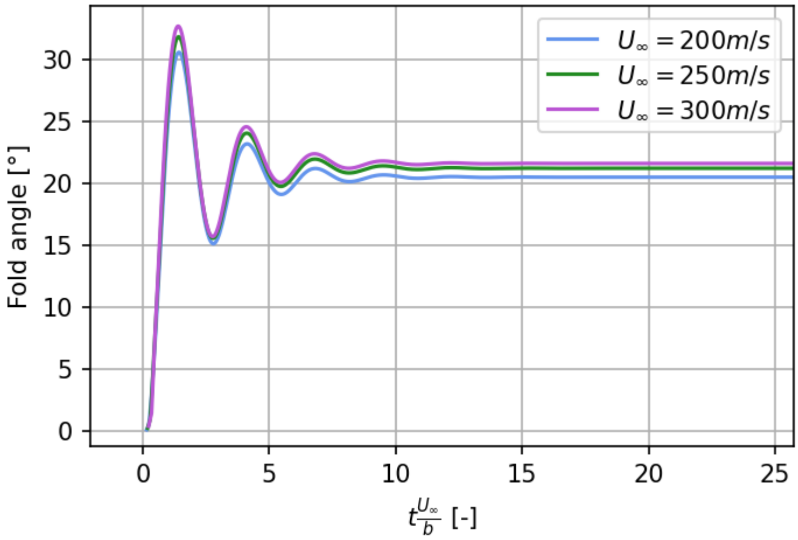

Figure 6.20: Evolution of the fold angle for different flow speeds at a same angle of attack.

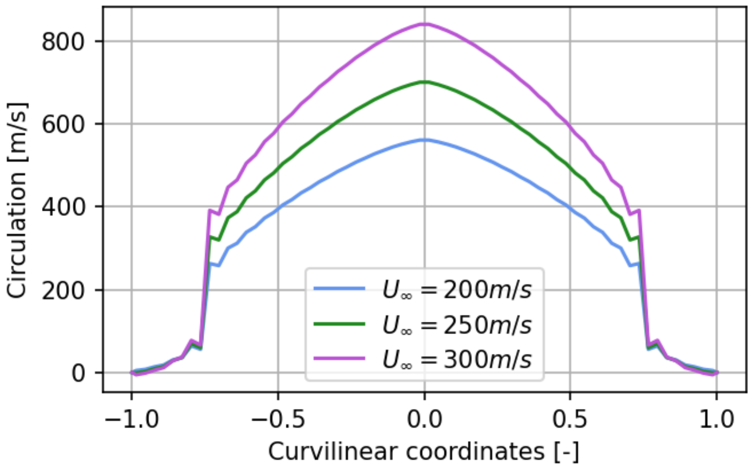

Figure 6.21: Evolution of the fold angle for different flow speeds at a same level of lift.

6.5.2 At a Same Level of Lift

At a same level of lift, the lift to drag ratio is strongly affected by the change in flow velocity. Changing the speed of the flow strongly modifies the angle of attack needed for the wing to generate enough lift to stay at level flight. At a higher angle of attack, the induced drag is highly increased, resulting in a lower lift to drag ratio.

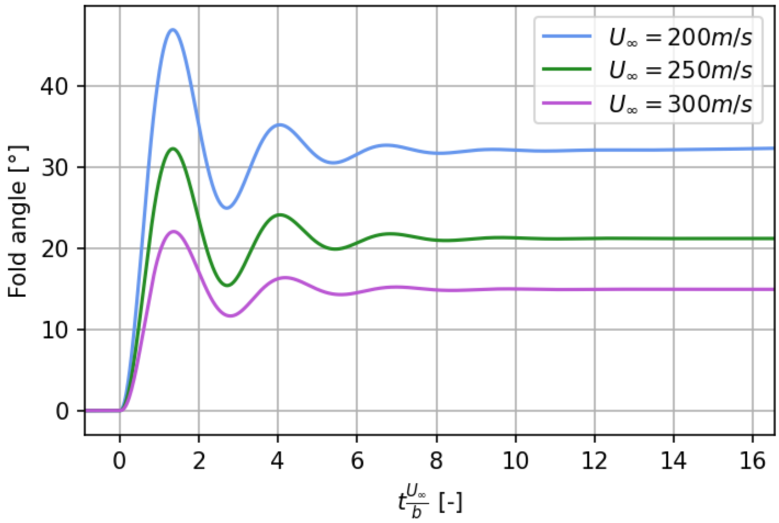

Figure 6.22: Evolution of the fold angle for different flow speeds at a same level of lift.

The overall dynamics of the wingtips stay the same, even though the coast angle is increased for lower flow speeds. A lower flow speed requires an increased angle of attack to achieve a same level of lift. The resulting evolution of fold angles depicted in Figure 6.22 therefore is in accordance with the results found in Section 6.4

6.6 Effect of the Wingtip Mass

The larger the wingtip mass m_{WT}, the lower the folding of the wingtip. Indeed, with a higher mass, the downwards gravitational pull on the wingtip is stronger. As can be seen in Figure 6.23, the dynamics do not benefit from an increase in mass. The number of oscillations and the time needed for these to die out are noticeably higher. In terms of the fatigue life of the structure, this in undesirable. Moreover, increasing the mass of the wingtip means increasing loads added far from the wingtip, resulting in the need for a stronger structure.

However, increasing the mass of the wingtip makes it possible to increase the lift to drag ratio. For a same flare angle, the coast angle is decreased, increasing the wingspan and decreasing the magnitude of the circulation drop at the hinge, resulting in less induced drag for a slight increase of lift (Figure 6.24).

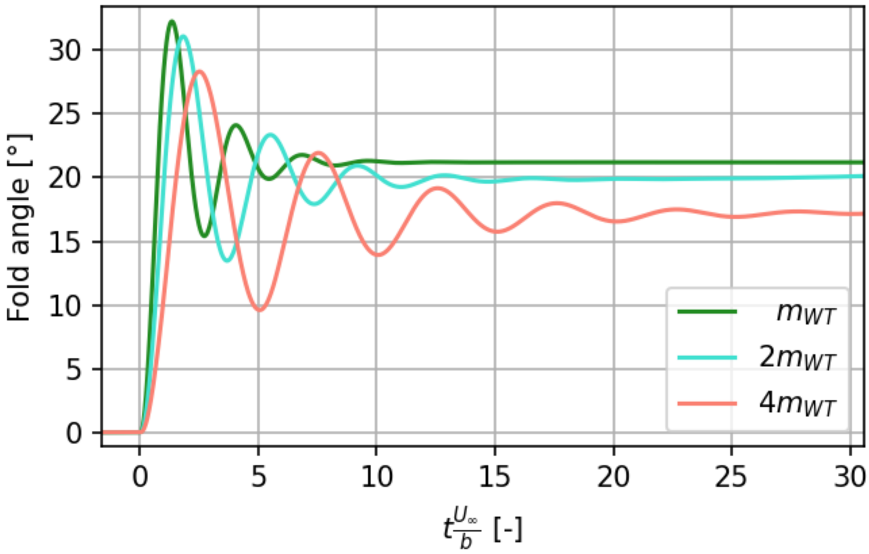

Figure 6.23: Evolution of the fold angle for different wingtip masses at a same level of lift.

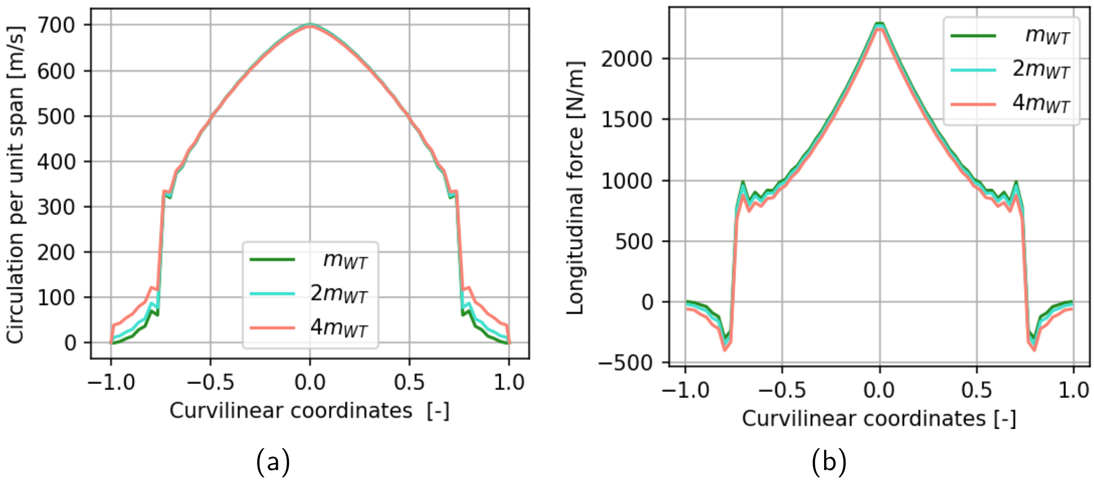

Figure 6.24: Distribution of (left) the circulation and (right) the drag force for different wingtip masses at a same level of lift.

6.7 Damping Coefficient

When the wingtip is free to move, a lot of vibrations are occurring throughout the whole flight. During cruise flight, when the wingtips are stabilized, small vibrations occur as the hinge is not fixed. Even bigger oscillations occur when the plane is subjected to larger perturbations such as turbulence, to a gust or to a wingtip release, if the hinges were initially locked. These vibrations and oscillations, if not limited properly, can enhance fatigue, accelerating the aging of the wing. Therefore, adding some damping to the hinge might be a good idea. However, it is important to find a suitable damping coefficient C, to make sure that the performance of the wingtip is not affected too much by the damping. The settling time should not be increased. It is also important to make sure that the load alleviation is still guaranteed and effective. Damping should not compromise the load alleviation capabilities of the FFWT.

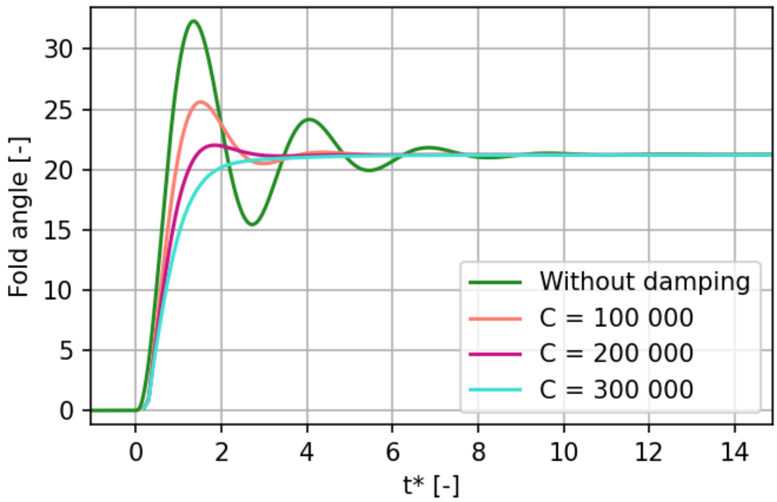

Figure 6.25: Effect of damping on the evolution of the fold angle

Different damping coefficients are compared, from which some are shown in Figure 6.25. A damping coefficient of $C = 2 \times 10^5 Nms/rad$ shows to have a satisfying behaviour. The settling time is decreased by about 30%, the overshoot and the amount of oscillations are limited. The response time is still relatively low, meaning that the hinge is still capable to respond quickly to the dynamics of perturbations such as gusts and turbulence. Higher damping coefficients might compromise the reactivity of the hinge. With damping, it is found the the wing root bending moment increases only with a negligible 0.1% compared to the case without damping. As will be discussed in Section 6.9, using a damping coefficient can be beneficial when facing turbulence.

6.8 Roll

The hope for the flared wing is to provide better manoeuverability than the fixed wing. The roll capabilities are assessed in different ways. First, the wing root bending moment endured by the different wing configurations are compared at given roll rates.

Later, the wings are subjected both to an external moment applied on the body and to the deflection of the ailerons. The main goal of these two tests is to assess the roll rates that the different wings can achieve, depending on the input.

6.8.1 Given Roll Rate

A first noticeable result is the evolution of the fold angle as a function of the roll rate. As the forces of drag and lift are not distributed evenly during roll, the fold angles do not evolve symmetrically. Instead, the wingtip on the inner wing moves up higher, while the outer wingtip is pushed to a lower fold angle.

The loads on the wings for the three wing configurations are compared at different roll rates: $p = 0$, $p = 5$ and $p = 10°/s$. These values are representative of the roll rates of large civil aircraft. As shown on Figure 6.26, the inner wing sees a significant increase of wing root bending moment, while the outer wing sees a decrease of wing root bending moment of roughly the same magnitude. This increase is proportional to the increase in roll rate. Overall, the WRBM values of the short and flared wings stay quite close to each other. The maximal WRBM on the flared wing, endured by its inner wing during roll, reaches values that are still below the ones that need to be supported by the fixed wing during level flight. With damping, the values of the wing

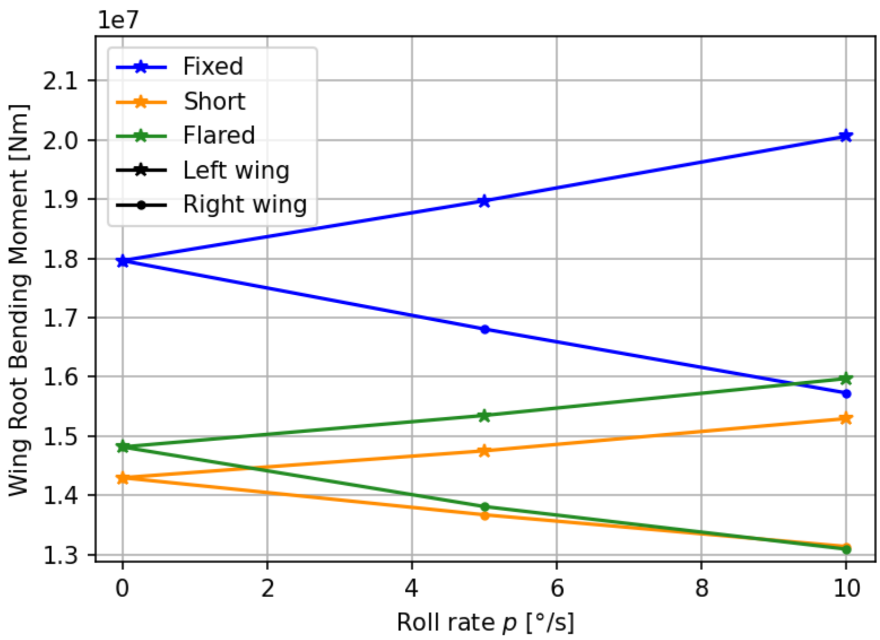

Figure 6.26: WRBM on inner and outer wing during roll at given roll rates.

root bending moment for the flared wing are slightly increased, but only by a negligible 0.3%.

6.8.2 Roll by Application of External Torque or by Aileron Deflection

For a same aileron deflection, or a same moment applied to the wing around the longitudinal axis, the three wing configurations achieve different roll behaviours.

Application of a Constant External Torque

Figure 6.27 shows the roll rate of the three configurations, normalized by the mean steady roll rate of the short wing, when the wings are subjected to an external torque around the longitudinal axis. It can be seen that the fixed wing reaches only 50% of the roll rate of the short wing, and that the roll rate of the flared wing oscillates around the one of the short wing. As described in Section 3.4, wings with a longer span suffer relatively more from roll damping. This explains why the fixed wing has a highly reduced roll rate, compared to the short wing. The flared wing, however, can recover most of its roll capabilities thanks to its flared folding wingtips. But when the wingtips are free to fold during the roll motion, they do not find a steady coast angle. Instead, they oscillate at a very low frequency. These oscillations are coupled to the oscillations that can be observed in terms of roll rate. This variation is found to be independent of the roll rate, but depends on the roll angle, with a period $T_\phi = 360°$. This effect might be due to the action of gravity on the wingtips.

When zooming in, Figure 6.28 is obtained, showing that the roll rate of the short wing also oscillates as a function of the roll angle, but with smaller amplitude and period.

Interesting to note is the range of roll angles for which the roll rate of the flared wing is higher than the one of the short wing. This comprises the typical range of roll angles achieved by large civil aircraft, going approximately from -45° to 45°.

Varying Aileron Deflection

The roll behaviour of the three main wing configurations have been assessed for a given pattern of aileron deflections. First, some time is given for the flow to settle and for the wingtips to reach their stable position. Then, the angle of attack linked to the aileron deflection is slowly increased from 0° at $t = 2s$ to 1° at $t = 4s$. At $t = 6s$ the aileron deflection is brought back to zero, over a time span of 2 seconds. From $t = 8s$

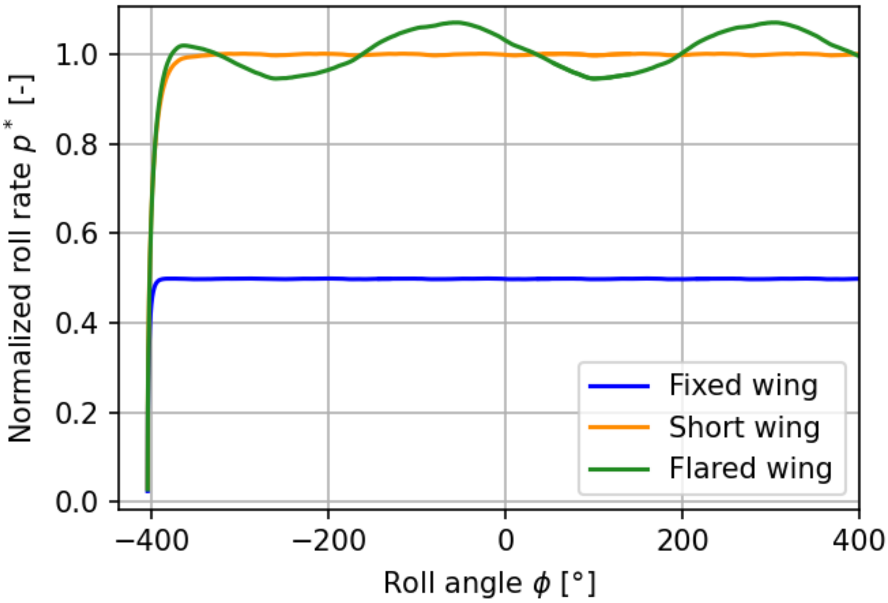

Figure 6.27: Normalized roll rates attained with a given external torque. Normalized by the mean steady roll rate of the short wing.

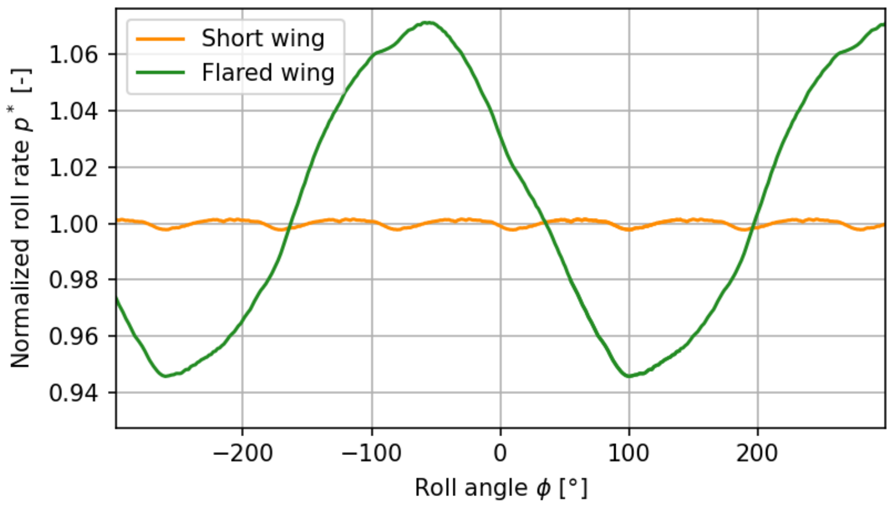

Figure 6.28: Zoom of the evolution of the roll rate in order to observe the oscillations on the roll rate of the short wing.

on, the roll controller is activated to bring the roll angle of the wing gradually back to 0° by making use of the ailerons. The resulting roll angles and roll rates are shown in Figures 6.29a and 6.29b respectively.

The behaviour of the short and flared wings are quite similar. The main difference between both is that the flared wing reacts slightly faster and stronger than the short wing. For the range of roll angles considered here, between -2° and 16°, this is in accordance with the result found when looking at a roll motion due to the application of a constant moment on the whole wing, where we found that the flared wing had a higher roll rate than the short wing.

Due to increased roll damping, the fixed wing is not able to achieve roll rates as high as the other wings for a same aileron deflection. A higher aileron deflection, or equivalently a higher torque, needs to be applied to the fixed wing for it to achieve a similar roll rate as the two other wings.

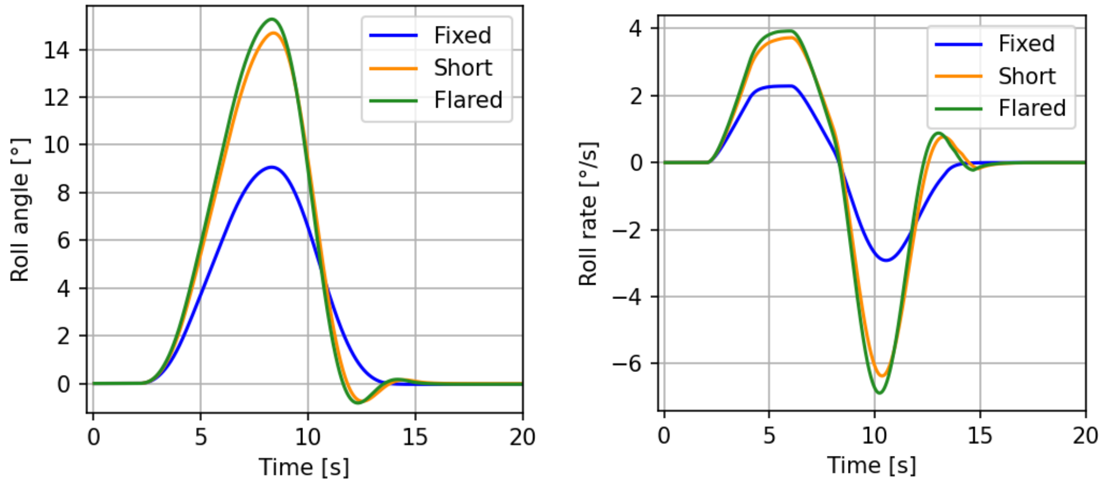

(a) (b)

Figure 6.29: Evolution in time of (a) roll angle ϕ and (b) roll rate p. Increase of aileron deflection from $t = 2s$ to $t = 4s$, decrease of aileron deflection from $t = 6s$ to $t = 8s$. Activation of roll controller at $t = 8s$.

6.9 Turbulence

As explained in Section 3.5, the turbulence is modeled using Mann Boxes. Two different intensities are modeled. From Equation 3.15 and the time evolution over time, the resulting turbulence intensities can be computed. The first Mann Box brings in turbulence with $T_I = 0.4\%$, the second box has $T_I = 3.9\%$. Both are compared with the case without turbulence, $T_I = 0$. Two degrees of freedom are liberated during this simulation: roll and pitch. Their values are regulated by means of the controllers defined earlier in Section 4.2.5.

The maximal wing root bending moments felt by the wings for the different wing configurations and turbulence intensities are listed in Table 6.2

	$T_I = 0\%$	$T_I = 0.42\%$	$T_I = 3.9\%$
Fixed wing	1.60×10^7	1.72×10^7	2.51×10^7
Short wing	1.27×10^7	1.37×10^7	1.97×10^7
Flared wing	1.29×10^7	1.43×10^7	2.05×10^7
Flared with damping	1.29×10^7	1.41×10^7	2.03×10^7

Table 6.2: Maximal wing root bending moments [Nm] to withstand during turbulence for different turbulence intensities T_I.

The WRBM values increased by 56% between zero turbulence and a turbulence intensity of 3.9%. The fixed wing thereby achieves wing root bending moments almost twice as high as the values for the short wing without turbulence.

Figure 6.30 shows the evolution of the wing root bending moment of the different wings over time for $T_I = 0.39\%$. The values for the short wing, and the flared wing with and without damping are all quite close to each other. The fixed wing, however, sees much bigger WRBM magnitudes. This is also the case for the turbulence at higher intensity shown in Figure 6.31 even though it is less clear there as the amplitude of the oscillations is bigger and there is thus more overlap.

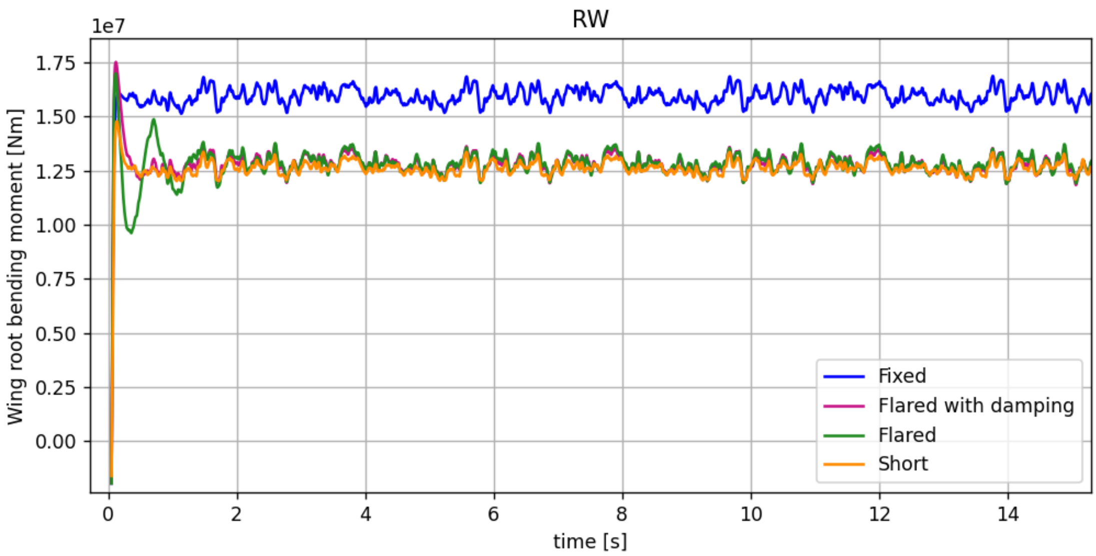

Figure 6.30: Evolution of the WRBM in time, in a turbulence with turbulence intensity $T_I = 0.4\%$

The maximal values listed in Table 6.2 do not take into account the peaks visible during the 2 first seconds of the simulations, which appear much larger than the other

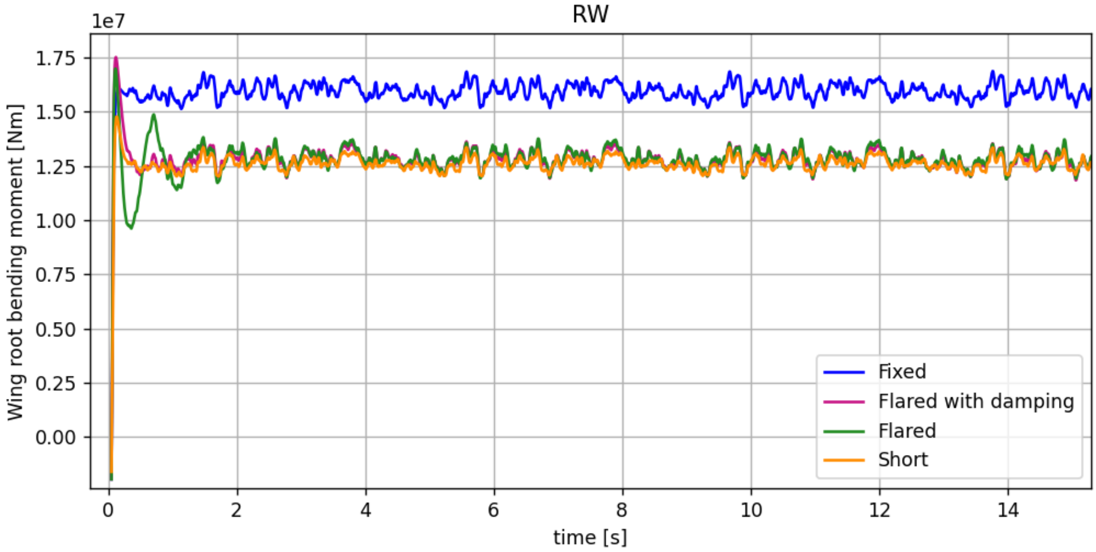

Figure 6.31: Evolution of the WRBM in time, in a turbulence with turbulence intensity $T_I = 4\%$

peaks for some configurations. In this analysis, the idea is to asses the load alleviation through the values of the WRBM during the phase of turbulence with completely free wingtips. The first seconds correspond to cases of wingtip release, but the analysis of this is left for a future work. Another aspect to explore is the behaviour of the wings subjected to turbulence when all the degrees of freedom the aircraft are freed. The next degree of freedom to liberate, after roll and the pitch, is the vertical translation. This would make it possible to have a better view on the (dis)comfort of the crew and passenger in the aircraft. However, the pitch controller was found not to be precise enough to keep the plane stabilized around a certain vertical position.

CHAPTER 7

Conclusion

Arriving at the end of this thesis, it is time to reflect on everything that has been done and what has not or has not yet been achieved.

According to recent studies, flared folding wingtip devices (FFWT) can be used to increase the wingspan of an aircraft without the need to give up the better roll rate and lesser loads of a shorter wing. To verify this, part of the thesis was dedicated to the comparison between three wing configurations: a long wing, a short wing of $3/4$ of the span, and a long wing with free folding wingtips with the hinges located at $3/4$ of the span.

These 3 configurations have each been modelled as an ensemble of lifting lines. Several models have been created in the process, gradually increasing the complexity and striving towards completeness.

To learn understanding about the behaviour of the flared wingtips, the impact of different parameters has been studied. This comprises the geometric angle of attack of the wing, the free stream velocity, the wingtip mass, the flare angle. From this, we learned that the flare angle should be a compromise between a high value, leading to an increased lift to drag ratio but higher bending moment contributions, and lower flare angles with less oscillations and faster stabilization of the wingtips. A flare angle of $20°$ is a good compromise.

Comparing different damping coefficients taught us that a high damping coefficient makes it possible to fight against the quick oscillations of the wingtips which might be detrimental to the longevity of the structure. Nevertheless, if the damping coefficient is too important, the response to quick perturbations like turbulence can be too slow, therefore losing some of the load alleviation capabilities of the FFWT.

With the chosen value for the flare angle ($\Lambda = 20°$), it was possible to compare the performances of the three wing configurations. First, the wing root bending moment (WRBM) for level cruise flight was considered. From this, it was already clear that the flared wing carried a little more loads than the short wing, but only 80% of the loads of the fixed wing. Then, the WRBM was compared for the three configurations at given roll rates. The resulting difference between fixed and flared was even bigger than in the case without roll.

The roll performances have also been assessed through applications of torques, both external and through aileron deflections. The result was a significant oscillation of the roll rate for the flared wing, and an important roll damping for the fixed wing.

Lastly, turbulence has been implemented using the Mann Turbulence Model. Again, the result was clear: the wing with free folding wingtips undergoes loads of similar amplitude as the short wing, while the maximal loads bared by the fixed wing are more than 20% higher.

One way to increase the relevance of the study is to increase the number of degrees of freedom of the wing. Here, only the degrees of freedom of roll and pitch are considered. With more developed controllers, it should be possible to add the degree of freedom of vertical translation, for example, without the aircraft moving too much up and down during turbulence.

Next to turbulence, it would also be interesting to consider gusts. The starting point for a gust load would be the flared angle with fixed hinge. With proper actuation of the hinge to obtain good well-timed wingtip release, it could be possible to assess how good the flared folding wingtip is for gust load alleviation.

Bibliography

[1] AlbatrossONE a revolutionary approach to aircraft wing design. https://www.airbus.com/en/innovation/disruptive-concepts/biomimicry/albatrossone. Accessed: 2021-09-29.

[2] A. Castrichini, V. Hodigere Siddaramaiah, D.E. Calderon, J.E. Cooper, T. Wilson, and Y. Lemmens. Preliminary investigation of use of flexible folding wing tips for static and dynamic load alleviation. *The Aeronautical Journal*, 121(1235):73–94, 2017.

[3] Andrea Castrichini, Vijaya Hodigere Siddaramaiah, Dario Calderon, Jonathan E. Cooper, Thomas Wilson, and Yves Lemmens. *Nonlinear Folding Wing-Tips for Gust Loads Alleviation*.

[4] Andrea Castrichini, Jonathan E. Cooper, Thomas Wilson, Alessandro Carrella, and Yves Lemmens. *Nonlinear Negative Stiffness Wing-Tip Spring Device for Gust Loads Alleviation*.

[5] Fintan Healy, Ronald Cheung, Theodor Neofet, Mark Lowenberg, Djamel Rezgui, Je Cooper, Andrea Castrichini, and Tom Wilson. Folding wingtips for improved roll performance. 01 2021.

[6] M.V. Cook. *Flight Dynamics Principles*. 01 2013.

[7] Federal Aviation Administration. wake turbulence. https://www.faa.gov/air_traffic/publications/atpubs/aim_html/chap7_section_4.html. Accessed: 2022-05-18.

[8] John D. Anderson. *Fundamentals of Aerodynamics*. 01 2011.

UNIVERSITÉ CATHOLIQUE DE LOUVAIN
École polytechnique de Louvain
Rue Archimède, 1 bte L6.11.01, 1348 Louvain-la-Neuve, Belgique | **www.uclouvain.be/epl**